

# 24-25 Hyperloop Global Structures FDR

Nikita Dolgopolov  
Sibley School of MAE  
Cornell University  
nd287@cornell.edu

Tokunbo Oshinowo  
Sibley School of MAE  
Cornell University  
too6@cornell.edu

Qing Yi Chen  
Sibley School of MAE  
Cornell University  
qc95@cornell.edu

Jonathan Distler  
Sibley School of MAE  
Cornell University  
jhd94@cornell.edu

26 March 2025

## 1 Introduction

This document discusses the structural systems of the Cornell Hyperloop pod. Following the establishment of the system requirements, simulations and hand calculations were conducted to assist in the design processes. This year's designs of the structures subsystems are building on the previous designs by extending them to a bigger scale and enhancing electrical subsystems integration. The chassis design is covered as well as the design of the battery pack mount and equipment for mounting other pods electronics.

## 2 Chassis Design

### 2.1 Chassis Design Criteria

This year's pod chassis has the same design as last year's. The primary reason for why we kept the design is to still conveniently host all of the pod's subsystems - the bigger electronics equipment like Variable Frequency Drive (VFD) and Battery Management System (BMS) take up a lot of space and the chassis we designed last year had enough space to accommodate for them all. Additionally, the lateral space in the chassis made mounting the Linear Induction Motor (LIM) feasible.

By utilizing the same chassis design as last year, we lowered the cost of development of the chassis, since no extra manufacturing needs to be completed. Furthermore, there is a good degree of flexibility in placing the pod's subsystems. This can allow for possible expansion into a second level for mounting electronics hardware. Additional constraints affect the sizing of the chassis:

- **Full Pod System Mass Constraint:** The pod mass has to be under 236 kg
- **Dimensional Constraint:** The pod must be under 10ft in length

### 2.2 Chassis Design Specifications

The chassis has a rectangular design form that is 9' (2.75 meters) in length and 14" (355.5 millimeters) in lateral width of the structure. The height of the chassis is fixed to 3" (76.2 millimeters). The structure consists of 2 longitudinal steel tubes with a wall thickness of 0.125" (3.175 millimeters), and

2 lateral tubes with the same thickness welded to connect the other pieces at the ends of the pod. Such configuration is very simple and satisfies the requirements of the system. Static loading hand calculations for a simply-supported beam and ANSYS FEA simulations were conducted to ensure the deflection of the middle of the chassis of less than 0.039 inches (1 millimeter) at the center of the pod under 200 kilogram distributed load. The real deflection is expected to be lower due to smaller actual mass of the pod (expected 130 kilograms) and a closer support points (wheels or electromagnets) to the center of the pod. The FEA simulation results as well as the chassis CAD are presented in Figures 1 and 2.

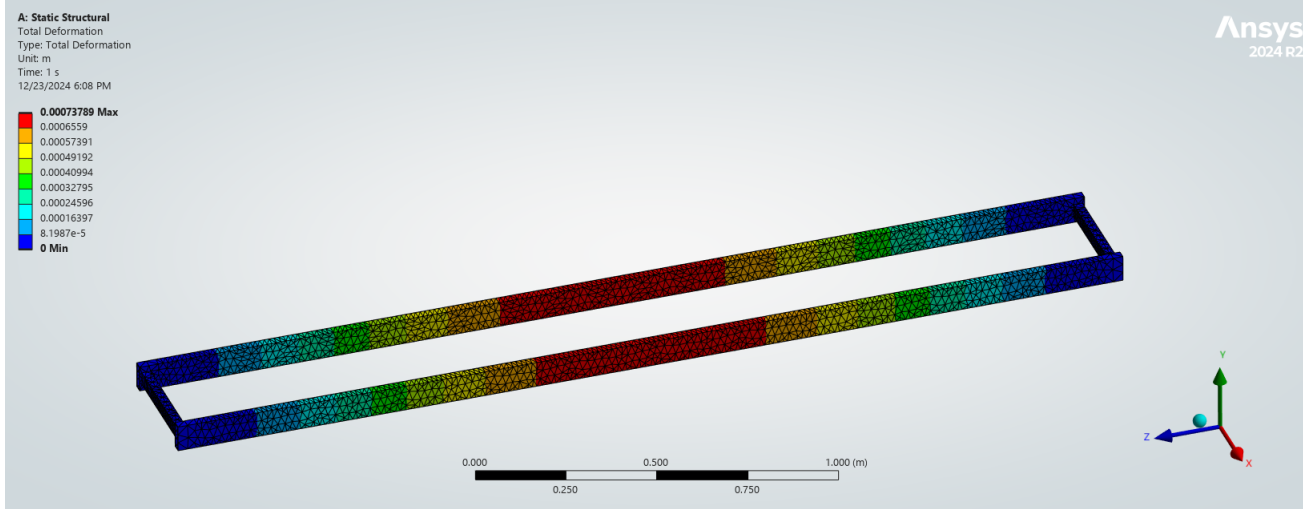


Figure 1: Chassis Deflection Study

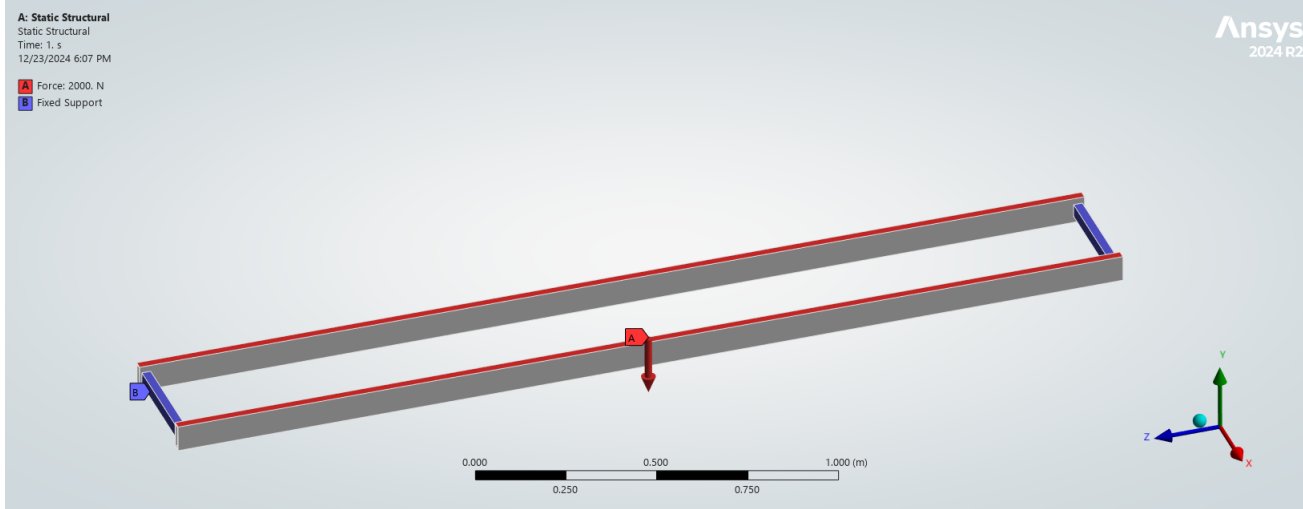


Figure 2: Chassis Loading Study

The extremely low deflection is achieved thanks to the high elastic modulus of steel, which is also quite dense. This results in a chassis mass of about 25 kilograms. ASTM A500 steel was used in the design due to its low price and ability to be welded internally by the school's welding equipment, which eliminated the need for outsourcing and saved about 2000 USD on the project. As a result, the total price of stock was 170 USD and the shipping cost was 280 USD. The cost of the project will increase when the holes in chassis will be drilled to mount the pod's subsystems. There are concerns about effect of the magnetic fields on the ferromagnetic structure of the chassis; however, these effects should not be too strong, as there are several inches of space between points of strong fields and the chassis and the fields decay very quickly with distance. The last concern is the corrosion possibility of the chassis, which will be addressed by coating the material with anti-corrosive paint.



## 3 Battery Pack Mounting and Electrical Enclosures Design

### 3.1 Battery Pack Overview

This year's Battery Pack will see many changes in its design. Based on each cell's relatively small resistance of 0.006 ohms, heat calculation results, and the estimated time that we are running the pod, we decided to omit a full battery-pack cooling system this year (Calculation 1 in Appendix Section A). However, considering the battery pack enclosure uses black acrylic (albedo approximately 0) to improve laser-cutting accuracy, it was advised from industry professionals that a partial battery-pack cooling system be implemented to negate reflected heat (Figures 8, 9, and 10). The blueprints involve creating a new enclosure that allows more space between the battery modules to make the wiring throughout the enclosure less congested (Appendix Section B). It has also been designed to be easily accessible. Like last year's enclosure, the Battery Pack will be enclosed in a configuration with 3 columns of battery modules, and the added air gap between columns makes room for convection currents to dissipate heat. The current design is easy to manufacture as it is simply an assembly of various subparts, most of which are easily manufacturable acrylic sheets (Appendix Section B).

### 3.2 Battery Pack Design

The individual cells are placed in spacing units and grouped together. The groupings together create the whole battery module which is 100 cells. This is then divided into 3 modules of 2 columns, of which two have 33 cells and one has 34 cells, totaling 100. Each of these blocks are held in place by an acrylic sheet on the top and one on the bottom. The bottom piece of acrylic acts as a flat surface for the batteries to rest on, while the top piece has a cutout of the 3 columns of modules for the batteries to prevent lateral movement. The top piece of acrylic is held 0.5" above the bottom piece of acrylic using unthreaded spacers; the battery groupings are shown in Figure 6 of the appendix. The height difference between the two pieces of acrylic was designed for three main purposes. The first purpose was so that there would be an air channel between columns of modules, which gives space for wiring and prevents an excessive amount of conductive heat from generating while maintaining the necessary electronics enclosure as stipulated in the rule book. Two slits are cut into the ceiling of the battery pack enclosure to further allow the battery pack to passively dissipate heat. The second was so that impulses delivered to the battery pack by track deviations and stopping would not cause the modules of battery packs to topple over. The full design and its components are in Appendix B. Finally, the columns of batteries allow for cold air to quickly move through the battery pack enclosure, removing excessive heat from the battery packs, as well as reflected heat from outside sources.

### 3.3 Battery Pack Manufacturing

The enclosure's modular design allows for swift assembly. The assembly components consist of support sheets which fix the position of the battery modules and a variety of 3D printed pieces and spacers which elevate the cutout sheet of acrylic, restricting lateral movement. Most of the non-load bearing structures, such as the unthreaded spacers seen holding the top piece of acrylic in Figures 3, 4, and 5, were intended to be 3D printed and fastened together using bolts and nuts. However, given the relatively cheap cost to purchase the pieces (the unthreaded spacers were \$ 1.97 each) and the expected precision of the spacers to work with already owned materials (i.e. M5 screws with a pitch thread of 0.8 threads/mm), it was thought that simply buying them would be a quicker and more precise alternative to 3D printing. The acrylic is intended to be cut using a laser-cutter. Having spoken with the laser cutting laboratory at Cornell University, a  $\pm 0.005"$  tolerance was used with our parts, given our use of material (acrylic) and our design specifications (rectangular cutouts throughout the acrylic pieces). The tolerance was accounted for and designed for as seen in Figures 4 and 6 of the appendix. The main change from previous iterations was making slightly smaller cutouts than intended (0.005 inches smaller than planned), such that excess material could be removed by hand, in the case of an under-tolerance, and the cutouts would be properly sized in the event of an over-tolerance. Finally, the enclosure will be mounted on the pod as one single component, sitting on aluminum 80/20 bars. The



---

bolts will pass through the middle-most part of the 80/20 bars and they will be fastened using T-Slot nuts, which allow for the bolts to be positioned flexibly. There are two lateral bars, to which another two bars are connected along the length of the chassis.

### 3.4 Secondary Battery Pack Design

In the event that the 100 cell battery pack is not fully functional in time for the competition, a secondary battery pack enclosure has been developed. The alternate system will use an AIMS 5000W Max Continuous, 240VAC output inverter, along with a 12V 300Ah LiFePO<sub>4</sub> Battery with a 250A BMS. The secondary battery pack design will also use the floor of the current battery pack enclosure to fasten the battery pack. Then, the team will use a pair of custom developed mounts to hold the battery pack against the acrylic in a secure position at the current location of the battery pack. Given the open-top design of the mounting system, it is intended that the heat will quickly dissipate throughout the interior of the aeroshell, meaning a cooling system will be unnecessary. The associated inverter will be placed on top of the current LIM system. It will be fastened to the system with a similar open-topped mounting system.

### 3.5 System Readiness Level

As of March 27th 2025, the CAD for the Battery Pack enclosure has been fully finished. The battery pack enclosure has been completed and tested using hand calculations and ANSYS evaluation (Figure 7), showing there is negligible stress throughout the battery pack with the given BMS load. The battery pack enclosure has been assembled. The only things that remain to do is to integrate the battery pack with its respective electrical components, which will ideally be completed by mid-April at the latest.

## 4 Battery Management System Design

### 4.1 Battery Management System Overview

A Battery Management System (BMS) that is outsourced will be used to regulate the temperature of each battery cell in the battery pack so that no cell surpasses 60 degrees Celsius. Furthermore, the BMS has its own cooling system that makes sure it is fully accountable over every battery cell while resisting overheating, keeping its own temperature below 80 degrees Celsius. Because of the BMS's integrated cooling system, an exterior cooling system will be omitted for the BMS.

### 4.2 Battery Management System Mounting

The BMS will be mounted on top of the battery pack enclosure to allow for more lateral space in the chassis and organization of wiring. Specifically, the BMS will rest on an acrylic sheet fastened to 20/20 bars that elevate the BMS above the battery pack (Figure 5). The acrylic sheet is designed with a sufficiently sized opening removed to allow wires to pass through, neatly connecting the battery cells and BMS together. Resting the acrylic sheet on 20/20 bars that form an arch over the whole enclosure is necessary due to the length of the battery pack enclosure and inadequate support of only acrylic sheet over the distance. The 0.25 inch thick acrylic top sheet is not strong enough alone to support the BMS over a length of roughly two feet, so having 20/20 bars supports prevents a fracture in the acrylic and averts a consequential collapse of the BMS. To connect the bars to themselves and to the floor of the battery pack enclosure, corner braces will be used and oriented so that they do not obstruct the battery modules. This enclosure can also allow for easy access towards battery modules because of the opening and hinges on the top edge of the prism. These hinges allow for the the enclosure to be swung open and held in place so there is no need for complete disassembly when completing tasks such as maintaining the batteries or wires.



---

## 4.3 System Readiness Level

As of March 27th 2025, the BMS mount CAD is completed. So far for hardware, the 20/20 bars have been cut and assembled together with corner braces. Minor changes may occur to increase accessibility of batteries through the BMS mounting, ensure working integration with the battery pack enclosure, and improve the overall efficiency of the design as assembly and testing occur.

# 5 Low Voltage Electronics

## 5.1 Low Voltage Electronics Overview

In addition to the BMS, there are various other low voltage electronics such as the Adafruit Ultimate GPS, Arduino Megas, and the HiLetgo HC-05 Bluetooth sensors. Since these electronics are delicate and provide great functionality to our pod, we decided to create enclosures and mounts so that they can be properly accommodated for.

## 5.2 Low Voltage Electronics Mounting

In order to make sure the electronics are mounted safely, this year we incorporated a designated "Electronics Center" for the micro controllers (Figures 11 and 12). Each of the micro controllers come with their respective plastic enclosures, and they are mounted into acrylic sheets that go into an aluminum electrical enclosure. Lastly, this aluminum enclosure is mounted into 2 different 3D printed pieces which help secure the entire assembly to the chassis. To manage the communication lines coming and going from the micro controllers in the Electronics Center, we will be using harnesses (which can group multiple wires together) to make our pod more organized. The snap-fit harnesses were not only designed with a snap-fit holder such that the harnesses can run across the length of the chassis, but also stay in place and not tangle.

This year, we will be using two of the Adafruit Ultimate GPS sensors and a singular HiLetgo HC-05 Bluetooth sensor. We will be placing them on the outside of our aeroshell so that the carbon fiber does not interfere with the sensors' signals. All of these electronics will have mounts that conform to the geometry of the aeroshell and will be mounted into the aeroshell with bolts and nuts.

# 6 Conclusion

In this paper, the design process of the Structures systems was outlined so that the manufacturing and assembly plans can be fully completed by May 22nd 2025. The future work will be focused on implementing the electronics system for the current battery pack enclosure to power the cooling system, as well as finalizing the open-top mounting system design in the case that Power Systems is unable to operate the 100 cell battery pack. Once these actions have been completed, we aim to begin testing of our subsystems in the Critical Design Phase.

## A

With data given from the battery specification sheet and expected maximum/minimum values for current and specific heat capacity of lithium iron phosphate batteries, the calculation of temperature change per unit time (seconds) comes out to be:

$$m = 75g \cdot 100 \text{ cells} = 7.5kg$$

*I = 30A (current is same when in series)*

*R = 6mΩ per battery*

$$R_{total} = 100 \text{ cells} \cdot 6 \times 10^{-3} \Omega = 0.6\Omega$$

$$Q = mc\Delta T = P \cdot t = I^2 R_{total} \cdot t$$

$$c = 825 \frac{J}{kgC}$$

$$I^2 R_{total} = (30A)^2 \cdot 0.6\Omega = 540W$$

$$\Delta T = \frac{I^2 R_{total}}{mc} \cdot t = \frac{540W}{7.5kg \cdot 825 \frac{J}{kgC}} \cdot t = \frac{0.087^\circ C}{s} \cdot t \text{ or } \frac{0.16^\circ F}{s} \cdot t$$

For example, this calculation of  $+0.16^\circ F$  per second the pod runs consecutively returns roughly  $28.8^\circ F$  in temperature change if the pod runs for three minutes (180 seconds) straight with zero break. With the amount of time we are expecting to run the pod, we conclude that a cooling system is not necessary for the full functioning of this year's pod design.

### Calculation 1: Battery Pack Heat Calculations

## B

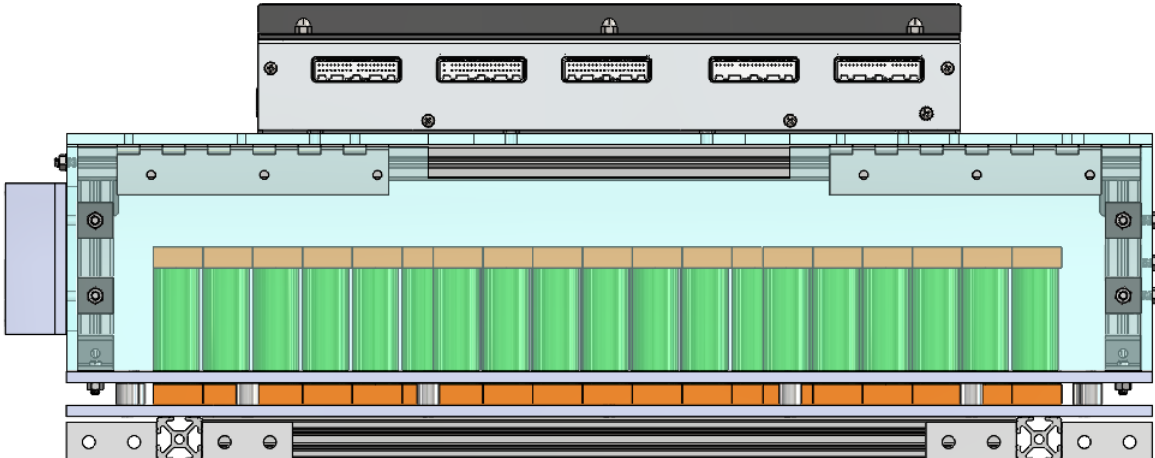


Figure 3: Battery Pack Side View

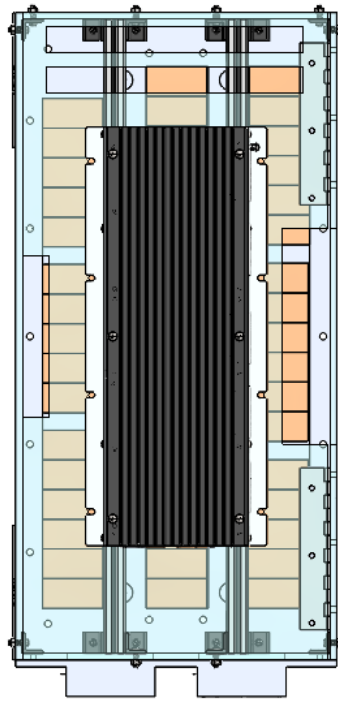


Figure 4: Battery Pack Top View

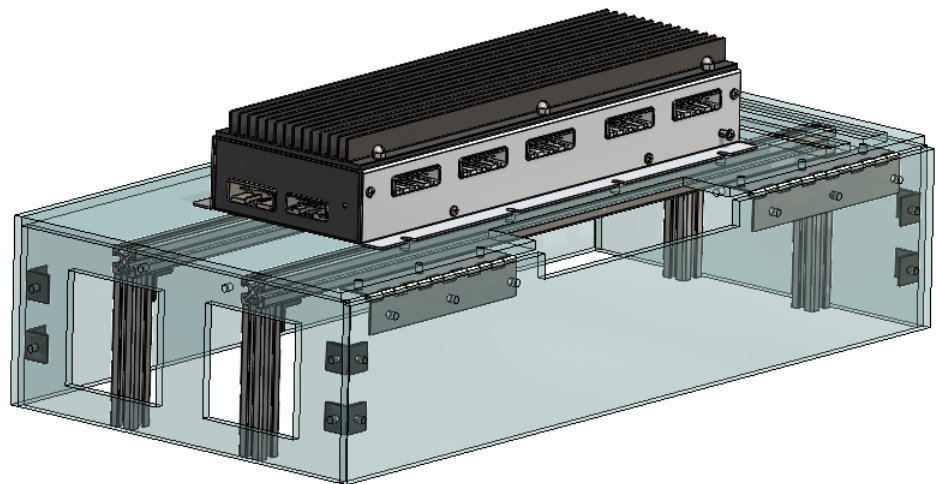


Figure 5: BMS Mount Schematic Isometric View

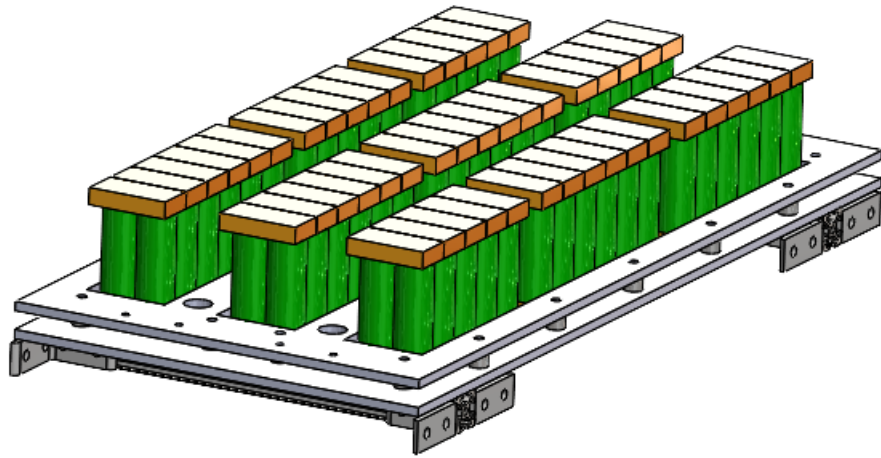


Figure 6: Battery Pack Isometric View

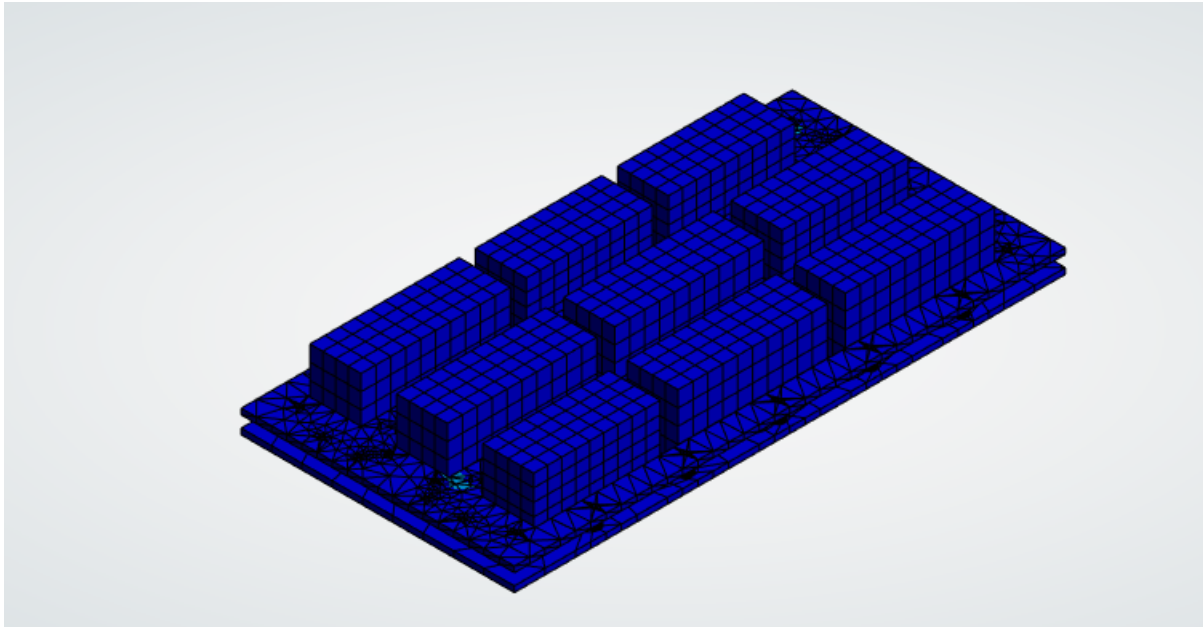


Figure 7: Battery Pack Isometric View with ANSYS Stress Test

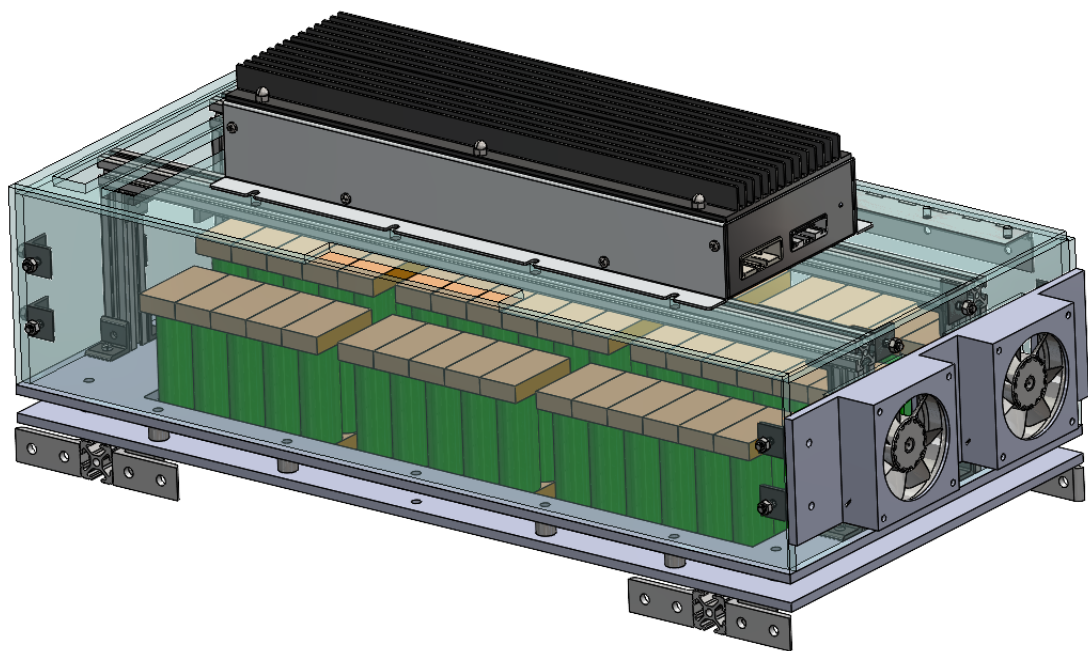


Figure 8: Battery Pack Enclosure Isometric View

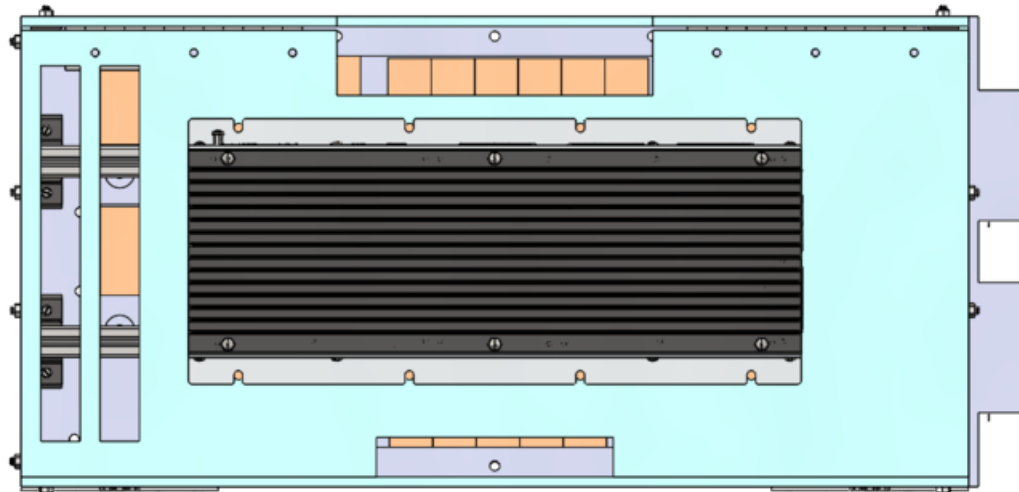


Figure 9: Battery Pack Enclosure Top View

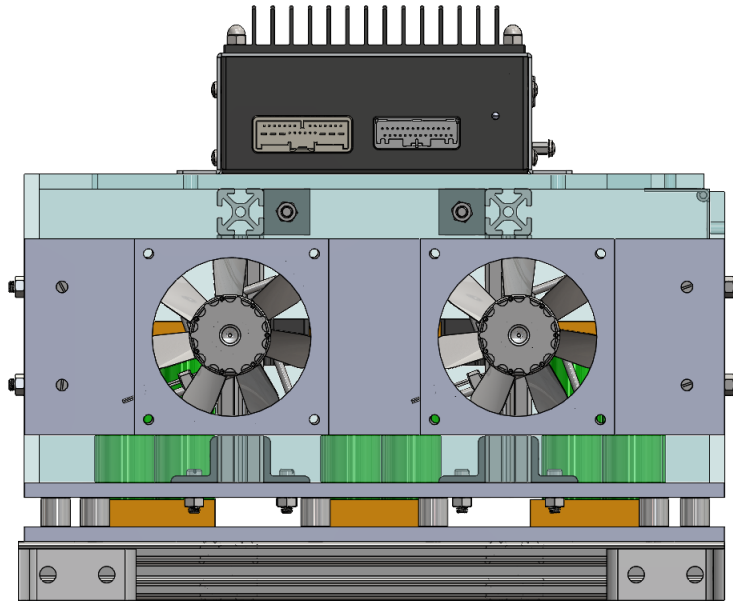


Figure 10: Battery Pack Enclosure Front View

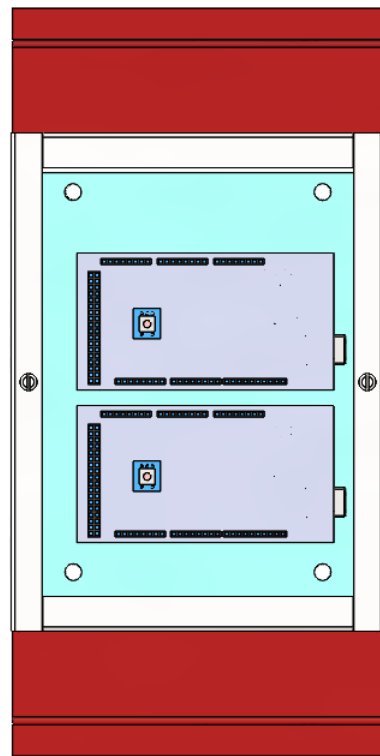


Figure 11: Electronic Center Top View

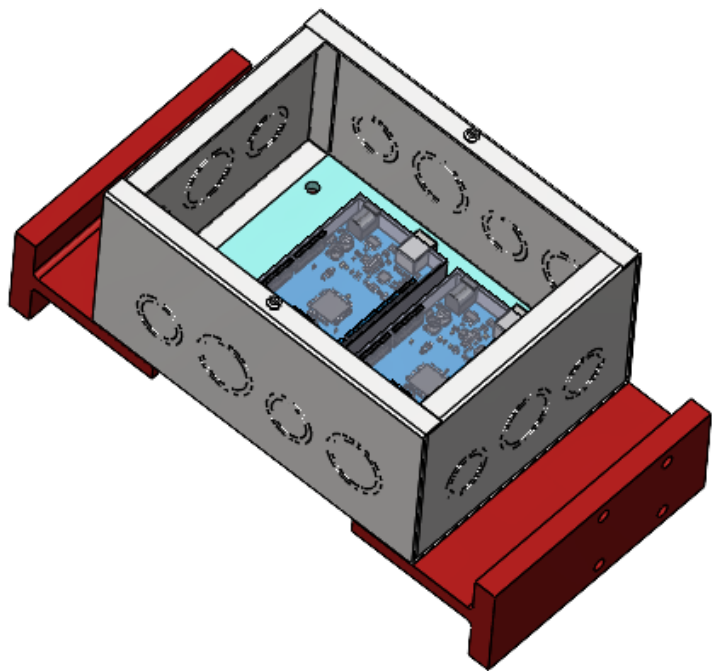


Figure 12: Electronic Center Isometric View

# 24-25 Hyperloop Global Braking and Pressurized Systems FDR

Shreya Anand  
Cornell University  
sa2228@cornell.edu

Carter McClintock-Comeaux  
Cornell University  
cpm225@cornell.edu

Madison Schaaff  
Cornell University  
mrs425@cornell.edu

Anubhav Nigam  
Cornell University  
adn38@cornell.edu

Nikita Dolgopolov  
Cornell University  
nd287@cornell.edu

29 March 2025

## 1 System Overview

### 1.1 Desired Functionality and Proposed Advantages

The mechanical braking system is necessary to bring the pod to a complete stop. When the magnetic braking system no longer provides sufficient braking force at lower speeds, or in the case of an emergency when there is no electricity in the pod to activate the electromagnets, frictional braking pads are automatically pushed against the top flange of the I-beam at a high enough pressure to stop the pod. The pneumatic actuation system is what ensures that these mechanical brakes can still be activated in case of a total system failure, as the airflow-controlling valve remains open even when power is unavailable. This specific system offers the added advantage of minimizing the duration of direct contact between the pod and the I-beam, thereby reducing potential structural damage to the track and the pod.

The magnetic braking system is intended to considerably slow the velocity of the pod under high-speed conditions using eddy currents generated by a switchable magnet that is turned from the 'off' position to the 'on' position. Electromagnetic brakes are particularly advantageous in that they provide significantly faster deceleration force at high speeds when compared to traditional friction-based braking systems as the produced drag force is a function of the vehicle's velocity. Additionally, electromagnetic brakes do not need to contact the I-beam, thereby minimizing damage to the track.

### 1.2 Principles of Function

The magnetic brakes work through Lenz's Law, which states that when a magnetic field changes, the induced current creates a magnetic field that opposes the change in the original magnetic field.



---

Here is Lenz's Law expressed mathematically:

$$F = \frac{v * B^2 * A * t}{p} \quad (1)$$

where  $F$  is the resulting force,  $v$  is the velocity of the pod,  $B$  is the magnetic field produced from the magnets,  $A$  is the cross-sectional area of the conductor,  $t$  is the thickness of the conductor, and  $p$  is the volume resistivity (1/conductivity). Lenz's Law predicts the behavior of eddy currents, which govern the magnetic braking system.

In this system, the magnetic field of the brake is constant in magnitude, and as the pod moves, the motion of the permanent magnets in the magnetic brake create a spatially changing magnetic field. The motion of these magnets induces a current in the track - this induced current creates a magnetic field which opposes the motion of the permanent magnets, and thus the pod. The brakes are switchable, meaning the magnetic field can be turned 'on' and 'off.'

The mechanical brakes operate on the conceptually simpler principle of kinetic friction. As two bodies slide past each other, intermolecular forces and irregularities in the shapes of the objects create a frictional force opposing the relative motion of the system. This drag force is proportional to the pressure applied by the sliding motion and the coefficient of friction between the two surfaces. The kinetic energy that the pod produces is related to the mass and velocity of the pod. It can be calculated by:

$$E_k = \frac{mv^2}{2} \quad (2)$$

The force of kinetic friction is represented by:

$$F_k = \mu \cdot N \quad (3)$$

Where  $F_k$  is the friction force,  $\mu$  represents the friction coefficient and  $N$  represents the normal force. The braking power provided by the mechanical brakes is therefore dependent on the pressure applied to the flange of the I-beam and the coefficient of friction of the material used.

## 2 System Specifications

### 2.1 Mechanical Braking

The mechanical braking system consists of four friction brake pads that are pneumatically actuated to the track in the case of an emergency or when the pod needs to come to a complete stop. The electric ball valve, which has three ports, adjusts its orientation to control the release of high-pressure air to the pneumatic cylinders. The fluid schematic is presented in Appendix A, while the comprehensive system diagram is provided in Appendix B.

Initiating mechanical brakes involves passing an electric signal to the valve, causing it to change its orientation from its resting state. This action allows high-pressure air to quickly enter the cylinders, enabling them to extend and apply a braking force to the track through the use of frictional material. In contrast, stopping the signal restores the valve to its resting state, closing the path to pressurize the cylinders to depressurize the system.

---

## 2.2 Magnetic Braking

The magnetic braking system utilizes opposing or matching polarities of magnets to switch on and off, and create a bulk magnetic field that is either contained within the brake ('off') or propagates outside of the brake ('on'). The system consists of a base and two rotating disks. Each disk has 4 permanent magnets arranged in a circle, lying on their sides. The base has two sets of 4 magnets arranged in the same manner. Figure 3 illustrates this system. In the 'off' position the polarities of the magnets in the disks and bases are alternating - this causes the fields to line up and propagate internally within the system. Turning a disk by 90 degrees makes the polarities of the magnets in the disk and base align to the 'on' position, which causes the fields to repel and propagate outwards towards the track. The disks are turned via a stepper motor and gears attached to the disks (see Figure 5).

The power setup for magnetic braking is as follows: the two two-phase stepper motors are driven by two drivers due to the current limits of the stepper motor drivers, which are powered by an e-bike battery. The cost of the system is around \$150 due to the price of the drivers and the battery. The weight of the power equipment is about 2.7 kg, while the weight of the two stepper motors is 7.4 kg. This would require additional structural consideration for the design of the brake mount. The weight of the whole system is also problematic, since this equipment alone contributes about 9% of the pod's weight. The drivers and the battery are mounted on an acrylic sheet right above the brakes, and the CAD assembly of the electrical system is presented in Figure 4 of Appendix C.

## 2.3 System Integration

The mechanical braking system will be integrated into the rest of the pod by attaching it to the chassis, as shown in Appendix B. This system will be placed in the back of the pod behind the battery systems. The magnetic braking system will be installed at the back of the pod, next to the pneumatic braking system.

# 3 Research and Timeline

In our exploration of the mechanical brake system, our team focused on researching pneumatic cylinders, specifically aiming to locate double-rod, double-action cylinders that act in opposite directions. However, we encountered challenges in finding suitable cylinders for the task such as being unable to procure the desired double-rod cylinders. Consequently, our team devised an alternative solution: converting the single action of a pneumatic cylinder into a dual action in the opposite direction. While this resolved our initial problem, it necessitated the incorporation of additional mechanical components into the system, leading to a more time-consuming machining process and added complexity to the mechanical braking system.

Furthermore, our team delved into addressing potential misalignment in the I-beam concerning the mechanical brakes. Two viable solutions emerged: one involved adding rollers to the part most prone to misalignment, and the other entailed designing the lower front part of the backing plate cylindrical, introducing a flange on the lower section, and extending the braking pad to cover this cylindrical part. You can see the design in Appendix C. Despite the challenges in research and design, our endeavors proved successful in refining the mechanical brakes.



---

This year's design for the mechanical braking systems remains similar to previous iterations of our team's pod; most of the new design work is related only to improving actuation methods and reducing overall complexity. In past years, the braking sub-team faced challenges with insufficient space and an inability to find pre-designed actuators that fit our particular constraints. Previous actuation systems involved actuators that were either discontinued before they could be ordered or did not fit into the overall design. Therefore, research on designing actuators from the ground up began over the past summer.

Early in the semester, time was spent refining other components of the previous year's braking system while also searching for a way to actuate our magnetic braking system. It was decided that stepper motors in the team inventory would be the most cost-effective method of actuating the magnetic brakes. Initially, an electrical ball screw linear actuator was planned to be used for the mechanical brakes, but this idea was scrapped in favor of pneumatics because of their ability to actuate after a cutoff power via the dead-man-switch method.

### 3.1 System Readiness Level

The mechanical brake system has achieved a commendable level of System Readiness. Through research and innovative problem-solving, our team addressed challenges in sourcing specific pneumatic cylinders. We successfully adapted by converting single-rod cylinders into double-rod, opposite-acting cylinders, although this added complexity to the mechanical components.

Additionally, efforts to enhance the system's robustness against misalignment in the I-beam were successful. Strategic design modification, including a cylindrical configuration with a lower flange and an extended braking pad, exemplifies our commitment to optimal performance.

Currently, the mechanical brake system is in excellent condition. We are scheduled to complete the final testing and integration of the mechanical braking system by mid-April. This positions the system as well-prepared for further advancements.

The magnetic braking system is past the prototyping process, and has a reasonable level of System Readiness. Based on the current timeline, the system should be fully integrated by the end of April. The final steps simply involve mounting and integration issues; the system has been tested and is fully operational.

### 3.2 Challenges and Future Design Iterations

Despite the progress made in achieving a commendable System Readiness Level for the mechanical brake system, certain challenges and considerations have surfaced for future design iterations. The adaptation of single-action pneumatic cylinders to dual-action configurations, while innovative, has introduced additional complexity to the system, potentially impacting its efficiency and maintenance. Striking a balance between functionality and simplicity will be crucial in future design iterations to ensure optimal performance and ease of repair and manufacturing.

Moreover, addressing potential misalignment issues with the I-beam, while successful, may benefit from further refinement. Ongoing assessments and tests will be essential to validate the effectiveness of the solutions introduced in prolonged use and varying operational conditions.

As we predicted, many unknowns initially clouded the results of our testing of the magnetic system. However, after extensive testing and prototyping, we are confident that our design is properly assembled to accomplish magnetic braking on a large scale. While final testing with the



---

pod is necessary to fully confirm the functionality of the system, we believe the rigorous testing protocol leaves little room for unexpected errors or behavior to crop up in the final integration.

## 4 Conclusion

This year's pneumatic brakes are an improvement of last year's design through mass-optimization and minor redesign to improve the manufacturing process. We also completely redesigned the magnetic braking system, due to our previous transformer-based design's failure under power constraints. Our novel approach appears to circumvent this issue, proving to be very effective with low power requirements. We look forward to seeing both systems functioning with the entire pod.

# Appendix

## A Fluid Schematic of Mechanical Brakes

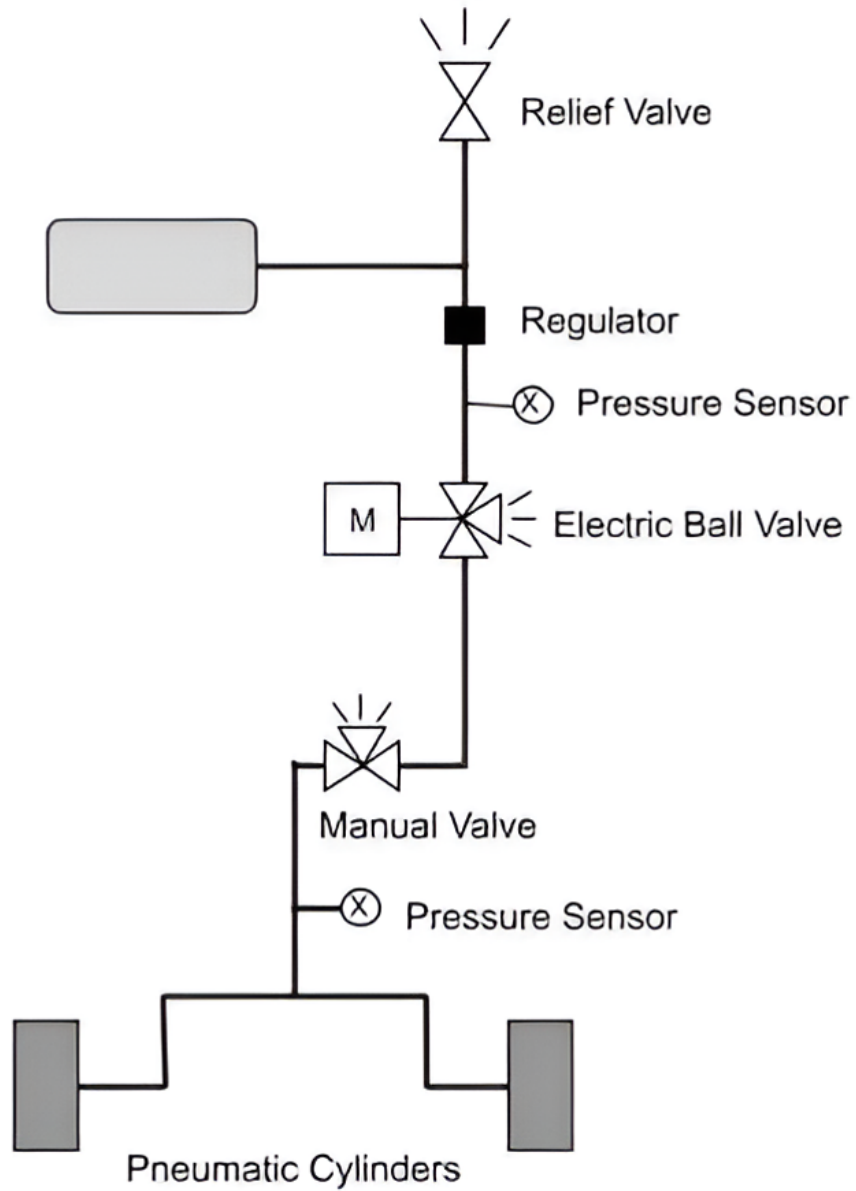


Figure 1: Pneumatic System Diagram

## B Mechanical System Integration

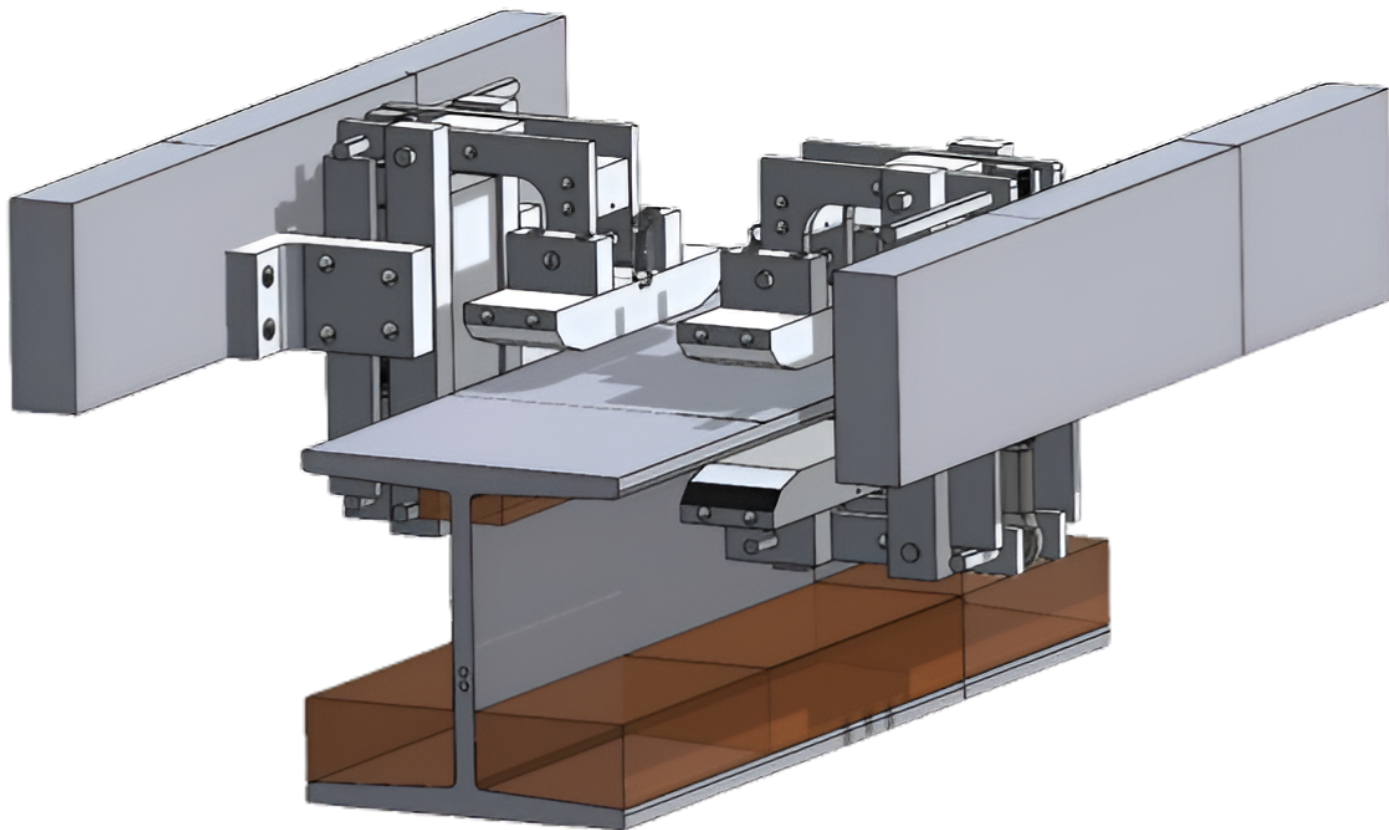


Figure 2: Mechanical System Integration

## C Magnetic braking system

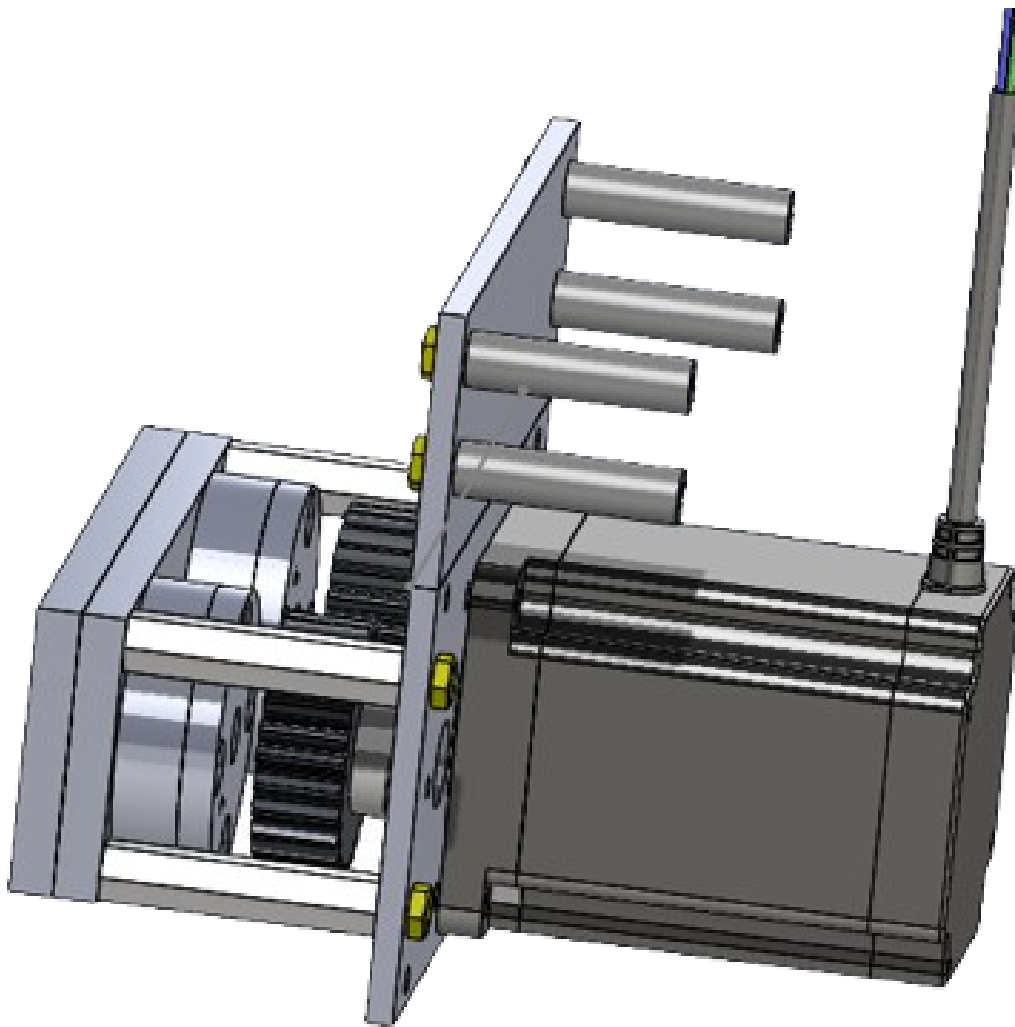


Figure 3: The Magnetic Braking System

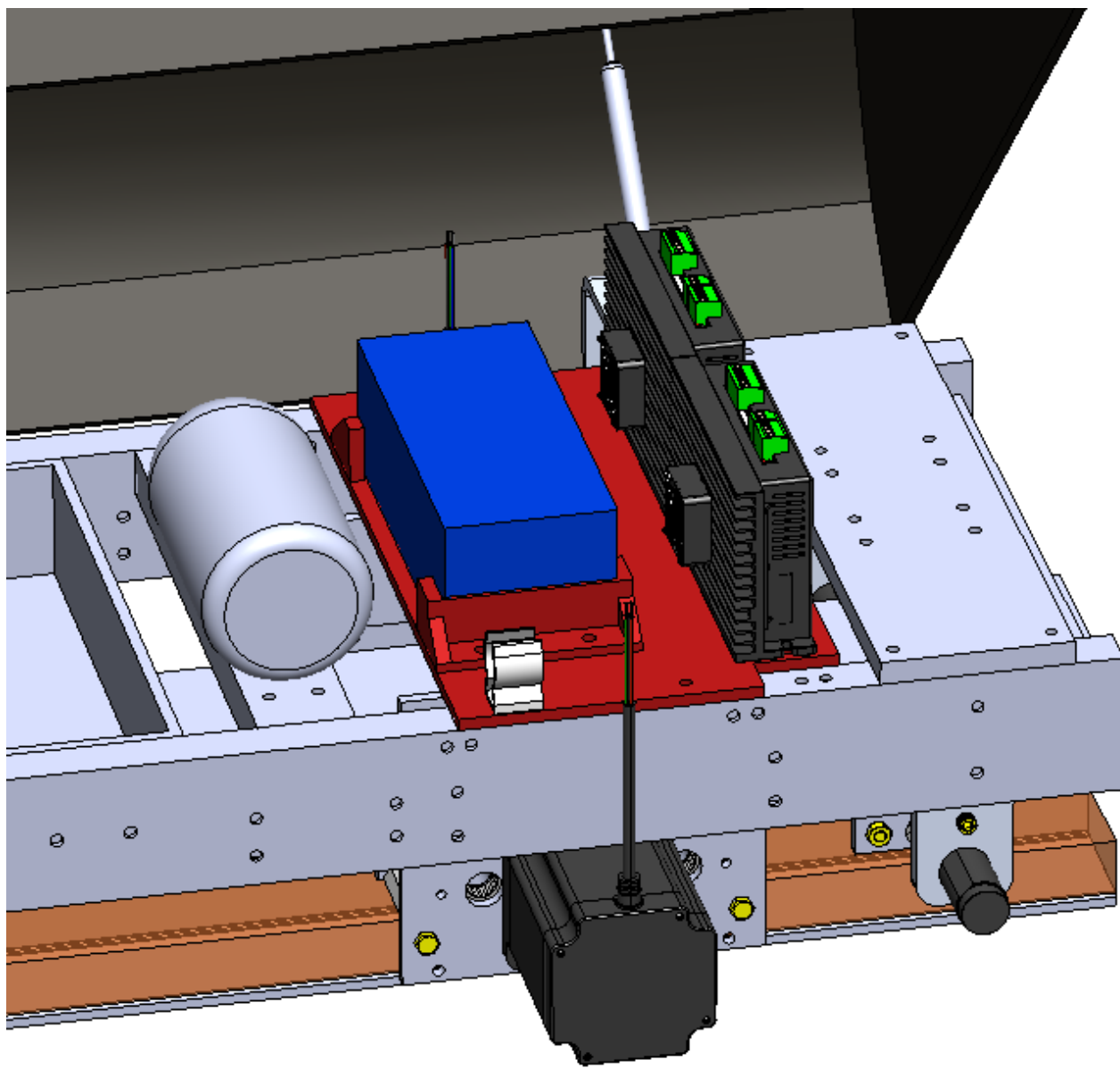


Figure 4: Electronics of Magnetic Braking System

# 24-25 Hyperloop Global Aeroshell FDR

Nikita Dolgopolov  
Sibley School of MAE  
Cornell University  
nd287@cornell.edu

Daniel Akinwale  
Sibley School of MAE  
Cornell University  
dda38@cornell.edu

Tokunbo Oshinowo  
Sibley School of MAE  
Cornell University  
too6@cornell.edu

29 March 2025

## 1 Introduction

This year's design of the Aeroshell is building on the previous design, which was built for a chassis that was about six feet long; making the Aeroshell a similar length. This year the chassis longer, so the Aeroshell length and subsequent geometry needed updating. Furthermore, there are new mounting developments and slight alterations to the timeline to account for manufacturing and mounting subassembly construction. These alterations and updates will be the focus of this paper.

## 2 Aeroshell Design

The internal dimensions of the pod this year are 9 ft long, 14 in wide, and about 1 ft tall. Thus, the Aeroshell will be 2 ft wide, 1.5 ft tall, and 9.5 ft long to account for its curvature. Its nose may later have slits near the sides to allow air to enter the insides of the pod to then be directed to internal systems that require cooling by ducts. This alteration; however, may be further into the future as no plans have been made to pursue this option for the moment. See in Figure 1 the completed design for the shape of the Aeroshell. This is an image of the intended shape of the complete Aeroshell.



Figure 1: Aeroshell

### 2.1 Aeroshell Design Overview

Understanding of the Aeroshell manufacturing process for documentation purposes and later usage was a major focus. With the nine-and-a-half-foot long design, fifteen pieces of high-density foam will need to be machined, put together, and prepared into the Aeroshell's mold. See Figure 3 in Appendix A. High-density foam will be used as a base for the mold because of its resilience and ease of use with acetone and sandpaper to create a smooth mold surface. The reason there are fifteen pieces is because the CNC mill our team used to cut our foam could cut pieces of up to size 2 ft by 2 ft by 0.25 ft. Thus, we had to take our shell design, use its inside profile, and slice it into pieces that could easily be CNC milled. With the given dimensions, we found that we needed fifteen pieces and determined that we could later adhere these pieces together using 3M Foam Spray Adhesive.

Materials:
High Density Foam
Duratec Surface Primer
Acetone
Fibre Glast 2000 Laminating Resin
Fibre Glast 2120 Epoxy Cure
Mold Release Wax
Mastic Sealant Tape
Vacuum Bag
Perforated Ply
Kevlar
Carbon Fiber

## 2.2 Aeroshell Manufacturing

With the above materials, we will create a high-density foam mold to graft the carbon fiber on top of. The assembly and preparation of the mold will likely take two weeks. The process for this is to attach all the pieces together with the aforementioned 3M spray, sand everything down to be smooth, then use Duratec Surface Primer to make a surface that is as smooth as finished wood. The grafting in question will consist of two layers of carbon fiber with one layer of Kevlar sandwiched between them. This particular configuration leverages the unique properties of each material; creating a composite that is both strong and resistant to impact, as carbon fiber provides high stiffness while Kevlar adds significant impact resistance. This combination effectively mitigates the weaknesses of each individual material when used alone. The layers will be coated with a 3:1 ratio of epoxy resin to cure, covered and vacuum sealed until cured. After that, the shell itself is complete. The shaping and curing of the complete Aeroshell should take one to three days. The manufacturing will be completed in January when the team returns from the winter break. See miniature prototype images in Appendix A, Figures 5-7.

Now our team has begun manufacturing the full-scale Aeroshell. We have been working for 3 weeks, doing 2 hours of work for 4-6 hours a week. Thus far we have placed and adhered all sixteen of our pieces together. We are in the process of sanding and patching cracks using 3M Bondo Body Filler. The biggest challenge so far has been to stop the formation of additional cracks while we are not actively working on and adjusting the mold. To fix this problem, our team ordered two sawhorses to hold the sides of the Aeroshell mold overhanging the table it sits on. In Appendix A Figure 8 is an image of the team working to fill cracks, sand, and prepare the large mold in question. In Figure 9 an image of one of the cracks that formed over time can be seen as well.

## 2.3 Aeroshell Mounting

This year we will attempt to alter the way we have previously mounted the Aeroshell to accommodate easy and fast maintenance of the pod for repairs or for showcase reasons. Instead of four brackets, each with two bolts that go through the Aeroshell into the bracket, the Aeroshell will be mounted around the outside of the chassis using five L-shaped Aeroshell Brackets than can be seen in Figure 4 in Appendix A. To allow for quick access to the various subsystems inside the pod, three gas struts are placed on the right side of the pod. One such gas strut assembly is depicted in Figure 2.

These three gas struts on the right side of the Aeroshell are mounted on top of the three L-shaped brackets on the same side, and two spring latch assemblies attached to two of the L-shaped Aeroshell Brackets on the left side of the pod. The latches can be quick-released, then the Aeroshell can be rotated open 45 degrees via hinges (also in Figure 2) attached to the L-shaped brackets on the right and suspended open by the gas struts during maintenance. The struts can then be disengaged, the Aeroshell lowered, and the latches put back into place. There will also be three 3D printed pieces, designed using the inner geometry of the Aeroshell, to distribute the force of each gas strut on the

Aeroshell and allow the gas struts to comfortably mount to the top of the Aeroshell. The force distributors will be printed with two holes in them that align with the gas strut bracket. The Aeroshell, each force distributor, and each gas strut bracket will then be fastened with two nuts and two bolts. Given the varying inside height of the Aeroshell, the gas struts' mounting pin will need to be mounted at different heights at each bracket. Getting the relevant components (gas springs, 3D printed parts, hinges, spring latches) will likely take two to three weeks. The construction of the sub-assemblies will be done during the same time period as the shaping and curing of the Aeroshell.

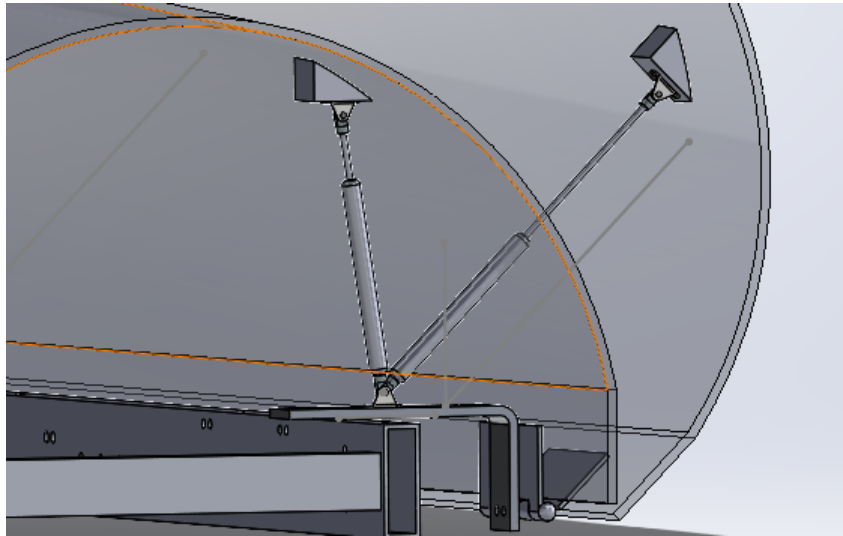


Figure 2: Gas Struts (Closed/Open Positions)

### 3 Conclusion

In this paper, the Aeroshell manufacturing process is outlined and relevant design tools are presented. The manufacturing and assembly plans were stated, as well as the timeline of the project. The work for the immediate future will focus on manufacturing the Aeroshell and its mounting subassembly in April 2025 and complete assembly between April and May 2025. Through manufacturing we are learning that we should make the mold more like a tub in which the carbon fiber is laid, that we should lay down vacuum bagging before working on the mold to avoid adhesion to the table, and that we should do everything in our power to create perfectly level surfaces to avoid the creation and propagation of cracks. Further than that, we will try to create some sort of system by which Aeroshell's of different lengths can be manufactured without having to create an entire new mold for each. The reason this is important is because the high density foam necessary for a mold of this size is two to three thousand dollars. To save the team from this troublesome expense in the future, a method for molds of different sizes appears necessary. Another future task is to ensure clear documentation for design and procedure when it comes to Aeroshell manufacture. Future members of the team should not have to completely learn the process on their own without the help of those who came before them. Whether that be in person teaching or clear documentation that does not leave them confused. This concludes the plans for the Aeroshell now and in the future to come.

**A**

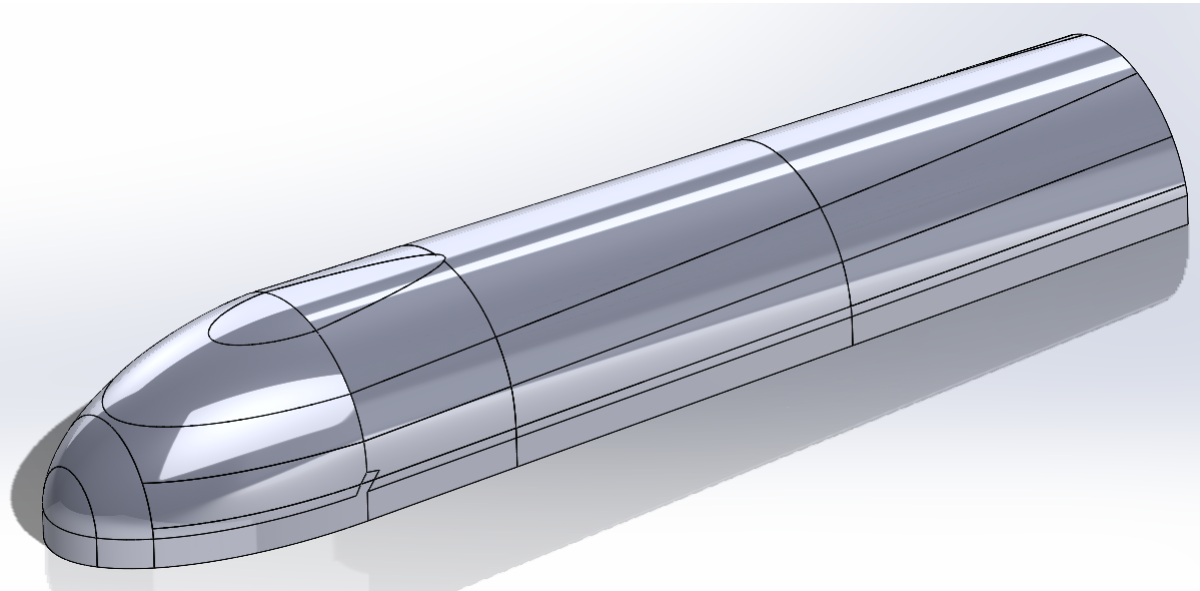


Figure 3: Assembled Aeroshell Mold

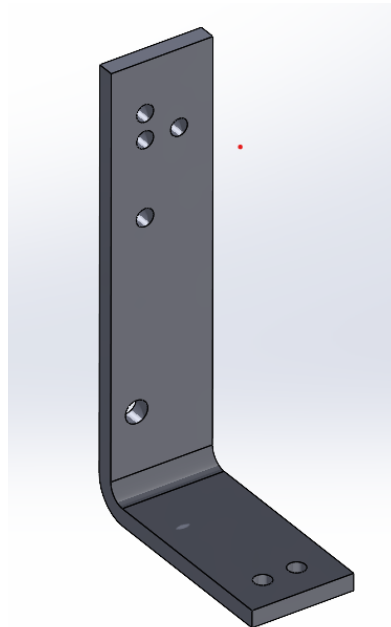


Figure 4: Aeroshell Support Brackets



Figures 5-7: Aeroshell Manufacturing Process



Figure 8: Large Aeroshell Sanding



Figure 9: Mold Crack

# 24-25 Hyperloop Global Guidance FDR

Salvatore Ciminello  
Sibley School of MAE  
Cornell University  
stc92@cornell.edu

29 March 2025

## 1 Abstract

The use of a guidance system allows for control along all three axes, the yaw, pitch, and roll directions. Our team's version of a Hyperloop pod has a guidance framework that utilizes two separate systems that work in conjunction to achieve stability in the translational and rotational directions. These systems are our horizontal guidance system and our vertical guidance wheels. This paper delves into the detailed specifications and design considerations of the horizontal and vertical guidance system for our pod as well as a detailed manufacturing process, ensuring compliance with the Hyperloop Global 2025 Rulebook and optimizing performance metrics such as stability, efficiency, and safety.

## 2 Introduction

The Hyperloop is a high-speed maglev train that is propelled through a vacuum tube at speeds exceeding traditional rail systems. In order for these trains to run safely and efficiently, they must stay on track and be well prepared for any disturbances that may derail it. The goal of our guidance system is to ensure our pod can stay on the track and dissipate all energy imparted to it due to an undulation in the track. This includes when the pod is accelerating, braking, running at maximum speed, and overcoming any disturbances within the track.

Our pod utilizes four shock absorbers that contact the track with castor wheels. These shock absorbers are located at the ends of the pod and are aligned symmetrically from one another about the track's center line. Additionally, four guidance wheels equipped with spring-loaded shock absorbers will be placed symmetrically about the pod's horizontal and vertical axes. This guidance system allows for the pod to resist and disperse any forces, or vibrations that it may encounter during operation.

## 3 Horizontal Guidance System Specifications

Our system must keep the pod on the track, while imparting no damage to the track. All parts must adhere to the tolerances, non-operation zones, and material specifications mentioned in the Hyperloop Global 2025 Rulebook. More specifically, the guidance system should be able to withstand a maximum 10° offset about its COM, and have a settling time of 5-10 seconds.

### 3.1 Functionality and Requirements

Our guidance system will utilize the same shock absorber assembly as last year but will incorporate large width wheels as compared to the previous years design which had ball bearings. The original

guidance system features a shock absorber designed to absorb a maximum energy of 147 J. The dynamics of this system can be analyzed using either Newtonian, Eulerian, or Lagrangian methods. Since a similar design of the system worked sufficiently well last year, we have a high degree of confidence in the system's ability to prevent interference between the pod structure and the track. The selection of spring stiffness was determined through force balance analysis and parameterized according to the desired time constant of the integrated position function. A isometric view of the system can be seen below:

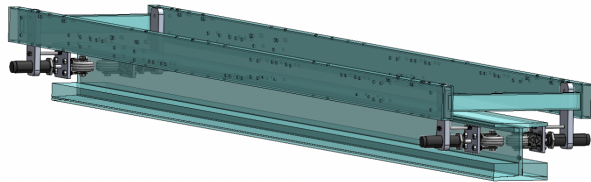


Figure 1: Isometric View of Horizontal Guidance System

In our initial approach of addressing the stability system, we looked at the dynamic equations of motion. Our dynamic assessment specifically centered on angular equations, anchored by a predetermined stability height of 3 millimeters. This height serves as a benchmark for the maximum roll angle, represented as  $\theta_{\max}$ , to avoid potential track interference. All computational evaluations were performed using MATLAB.

### 3.2 Equipment

Two critical elements of the stability system were scrutinized: the lateral displacement and the roll motion of the pod (Figure 3). Improving from last year, we are integrating guidance wheels on our current design as opposed to ball bearing, on the current shock absorber system.

As shown in the Appendix, at the beginning of the semester we derived a new governing equation for the motion of the pod about the roll direction. Using a Newtonian dynamics approach, the first step was defining an inertial and non-inertial coordinate systems. The second step was modeling the pod's movement  $\theta$ , while the third step was summing the applied forces for the spring-mass dampers, and applying that to Newton's Second Law. The full derivation of this governing equation is further expanded on Appendix B. Such equation yielded was:

$$\ddot{\theta} = \frac{(-2h^2 b \cos^2(\theta) \dot{\theta} - 2kh^2 \sin(\theta) \cos(\theta))}{I}$$

This equation gave us the motion of the pod as a function of two parameters,  $k$ , the spring constant, and  $b$  the damping coefficient. As a way to save on costs of buying new shock absorbers, we back tracked from the current shock absorbers, converted the energy capacity to individual  $k$  and  $b$  values, then simulated the motion of the pod in MATLAB using the governing equation above. The graph produced can be found here in Figure 5.

From product specification we determined the shock dispels 147 joules from the pod's motion per shock stroke. Counting for the max overshoot  $\theta$ , and the energy needed to be stored in the shock at that offset, we determined this dissipation rate is more than enough to accommodate our necessary settled time for the pod to go back to an equilibrium state.

After determining our current shock absorbers are a good fit for our current system, we decided to redesign the contact face of the shocks to the flange of the track. In a effort to increase the leverage

the stability system has to move the pod back to equilibrium, we decided to increase the width of the contact face of the rotating fixture to the I-beam. This led to us replacing our old ball bearing design with a wheel dependent design. This new design can be found in Figure 2.

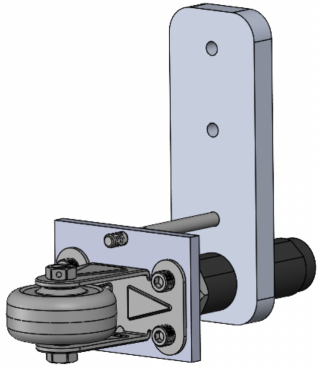


Figure 2: Shock Absorber Assembly

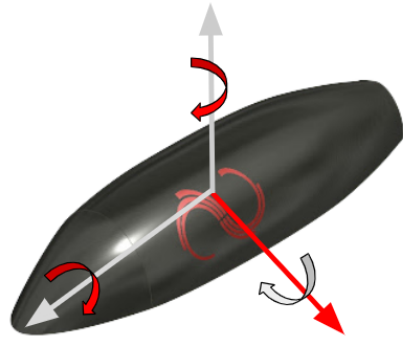


Figure 3: Stability Directions

### 3.3 Manufacturing and Purchasing

Since the guidance system is simply being redesigning, there is just a few steps that are needed to be taken before the system is ready.

On the manufacturing side four aluminum stock plates need to be milled down, one per guidance module, which will be fitted to the back of the purchased caster wheels, and screwed into the tip of the shock absorber. Following that, the previous years part that connected the shock absorber assembly to the chassis will also be modified slightly, by milling in a small hole. This small hole will connect this part to the caster wheel's holder, so that the whole assembly wont be free to rotate.

For the rest of the system assembly parts such as the bolts will be purchased, and the caster wheels we already have in stock. The purchasing/cost table for the remainder of the system assembly can be found below:

Description	Source	Unit Price	Quantity	Total Cost
Socket Head Screw 1/4"-28	McMaster-Carr	\$7.45	2 Packs	\$14.9
1/4"-20, 3-1/2" Bolt	McMaster-Carr	\$14.81	1 Pack	\$14.81
1/4"-28 Nut	McMaster-Carr	\$6.25	1 Pack	\$6.25

For a more exact plan for assembly, the first step is to dissolve the current adhesive bonding the shock absorbers to the previous years design using some industrial epoxy remover. Following that, the two items per module (eight in total) that need to be milled will be machined, then the shock absorber will be re-epoxied to the newly milled parts. After that the parts will be assembled using the nuts and bolts outlined in the purchasing sheet.

## 4 Guidance Wheels Design Specifications

While the shock absorber and wheel system provides stability along the yaw and roll axes (Figure 3), we still require guidance wheels to offer vertical support to our pod. The guidance wheels must ensure that the pod stays on track, and must disperse any applied forces or vibrations imparted onto the pod due to an vertical irregularity in the track.

## 4.1 Functionality and Requirements

The guidance wheels that were used in previous years were able to effectively maintain our pod on the track, but their rigid design meant that any track irregularities directly impacted the pod. This year our team has been looking to mount our pod with rigid castor wheels that contain spring loaded shock absorbers to mitigate such disturbances. By modeling the system as a second order system we were able to devise possible spring constants and damping coefficients that best fulfill this role.

## 4.2 Equipment

The vertical guidance wheels will feature four rigid castor wheels, symmetrically aligned along both the horizontal and vertical axes of the pod. An example configuration, showing one side of the assembly in contact with the I-beam can be found in Figure 4. This configuration aligns with the initial setup outlined in the Wheel Configurations section of the Canadian Hyperloop Conference Rulebook 2025.

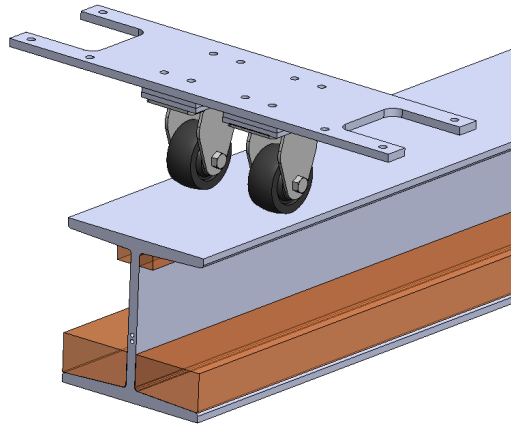


Figure 4: Vertical Stability System

To determine the essential spring constant and damping coefficient for our guidance wheels, our team conceptualized the system to mirror a car suspension. This approach enabled us to utilize the equation derived from the MathWorks documentation on Automotive Suspension:

$$F_f = 2K_f(L_f\theta - (z + h)) + 2C_f(L_f\dot{\theta} - \dot{z})$$

Where  $F_f$  denotes the upward force exerted on the pod by the front suspension,  $K_f$  is the spring constant of the front suspension,  $C_f$  represents the damping rate of the suspension, and  $L_f$  indicates the horizontal distance from the pod's center of mass to either the front or rear suspension. The symbol  $\theta$  signifies the pitch angle, and while its time derivative is represented by  $\dot{\theta}$ . Additionally,  $z$  corresponds to the vertical displacement resulting from a bounce. Conclusively,  $h$  designates the height of the track.

In order to determine the most effective spring constant and damping coefficients, we must make assumptions about the various conditions, such as the maximum vertical height  $z$  must not exceed 3 millimeters, and that the track's height will be treated as ground level, making  $h = 0$ . Additionally, the guidance wheels are to be placed approximately two inches from the front and rear ends. Once the values of  $L$  and  $z$  are decided, we can determine  $\theta$ , using basic trigonometry. Once these values were finalized our team tested different values of  $K$  and  $C$  to see which give the most fitting values of  $F$ .

## 4.3 Manufacturing and Purchasing

Since this vertical guidance system was more than sufficient for last year's competition, the team has decided to not change the system at all. Currently, the only plans we have for this system will be to integrate it onto the new chassis, then if needed, small washers will be implemented to either increase or decrease the height of the system. Besides that all the manufacturing and purchasing for this system was completed last year, so no more is needed for this coming year's competition.

## 4.4 Challenges

The primary challenges in designing the guidance wheels stemmed from time constraints and the simultaneous development of various subsystems. This concurrent design process made it difficult to accurately determine a few parameters of the pod's, like the center of mass, moment of inertia about the roll direction, and the lever arm for the guidance module, so estimations had to be made.

# 5 System Readiness Level

This timeline relates specifically to the guidance system, and lists the progression of designs through the Spring semester. This has a major focus on the completion of testing of the assembly early in the semester:

Spring 2025	March	April
Guidance Timeline	Dissolve Adhesive and Machine Remaining Parts	Final Assembly

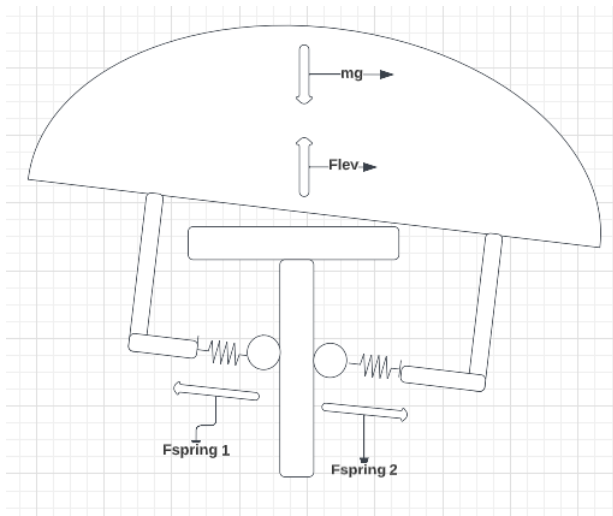
Overall this system is nearly complete due to its previous years performance, and the design just mildly being tweaked to optimize settling time.

# 6 Conclusion

Because the horizontal guidance system was previously used and performed well, there are not many changes to be made aside from verifying shock absorber capabilities, and replacing ball bearings with wider wheels. Testing plans are currently in place to test the ability of the shock absorber assembly to overcome a track displacement. This is being modeled as a step displacement, and the goal is to ensure the guidance system can overcome this maximum step, along with the maximum  $\theta$  offset.

Future design iterations of the guidance wheels and horizontal guidance system will likely stay as is from a design perspective, but there could be changes to system constants. For instance, the necessary spring constant and damping ratio of the shock absorber is heavily dependent on the pods mass, so if this value were to drastically change, the shock absorber selection would also change. We have also considered the idea of a more traditional rail follower system. The rail follower is a much more rigid design, but because the track is a straight path, and the pod's center of mass lies directly above the center of the track, we are not as concerned about rolling. In the future if the competition changed to incorporate a curved track, a rail follower method would be more advantageous to integrate.

## A System FBD

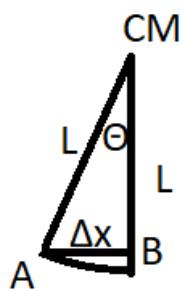


Inspection of the FBD, shows us that about the roll direction, the only forces we are concerned about is the spring force and damping force, represented by the symbol  $F_{\text{spring} 1}$ , and  $F_{\text{spring} 2}$ , in the above figure. This brings us to the follow conclusion that:

$$\sum F_x = K(L - \Delta x) + b\dot{x} - K(L - \Delta x) + b\dot{x} \quad (1)$$

## B COM Derivation

The following diagram allows to express  $\Delta x$  in terms of  $L$  and  $\theta$ . CM - center of mass of the pod, AB is the distance by which each spring compressed, and B - point of spring force application before the tilt.



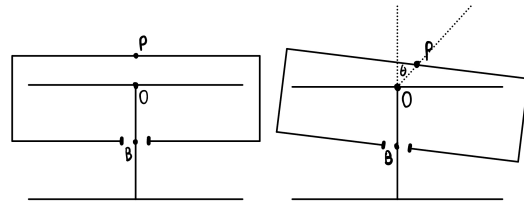
The following equation is obtained. It is assumed that even with roll of the pod spring force will be applied horizontally, which makes angle A-

B-CM equal 90 degrees.  $\theta_{\max}$  is expressed in radians.

$$\Delta x = L_{\text{com}} \sin\left(\frac{\theta_{\max} \times 180}{\pi}\right) \quad (2)$$

## C Coordinate System Definition

To move forward with the derivation of the roll motion of the pod we need to establish an inertial and non-inertial body following frame. Below is a figure that shows the approximation of the body, and its movement.



Where  $P$  is modeled as the top of the body's aeroshell,  $O$  is our inertially fixed point in the center of the track,  $B$  is the contact point of the shock absorber, and  $\theta$  is the degree at which the top of the aeroshell rotates with respect to  $O$ .

## D Kinematics and Integration

Since we were able to define our coordinate system we can now model the kinematics of the pod. The follow equations describe the position, velocity, and acceleration of the body with respect to the frames of reference.

$$r_{P/O} = h\hat{e}_r = h(\hat{e}_x \sin\theta + \hat{e}_y \cos\theta) \quad (3)$$

$$v_{P/O} = h\dot{\theta}\hat{e}_\theta \quad (4)$$

$$a_{P/O} = h\ddot{\theta}\hat{e}_\theta - h\dot{\theta}^2\hat{e}_r \quad (5)$$

With the Kinematic Equations of the body defined, we can now use the summation of the forces, our defined coordinates, and the definition of torque to get a differential equation relating angular acceleration, to our forces.

$$I\alpha = r_{P/O} \times \sum F_x \quad (6)$$

$$I\alpha = h\hat{e}_r \times (2b\dot{x} - 2k\sin\theta h)\hat{e}_x \quad (7)$$

Since  $\alpha$  is the same as  $\dot{\theta}$  in this case, we can rewrite this equation to a more familiar form.

$$I\ddot{\theta} + 2h^2b\cos^2\theta\dot{\theta} + 2kh^2\sin\theta\cos\theta = 0 \quad (8)$$

A numerical approximation using ODE45 in Matlab could then be used on such a differential equation to simulate the response of the pod overtime. MatLab's ODE45 is a method to numerically solve complex differential equations through numerical approximation as opposed to solving the equation outright. It is to be noted all of these variables are constants, except  $K$  and  $B$  which we are testing for due to the shock absorber.

## F Simulation Results

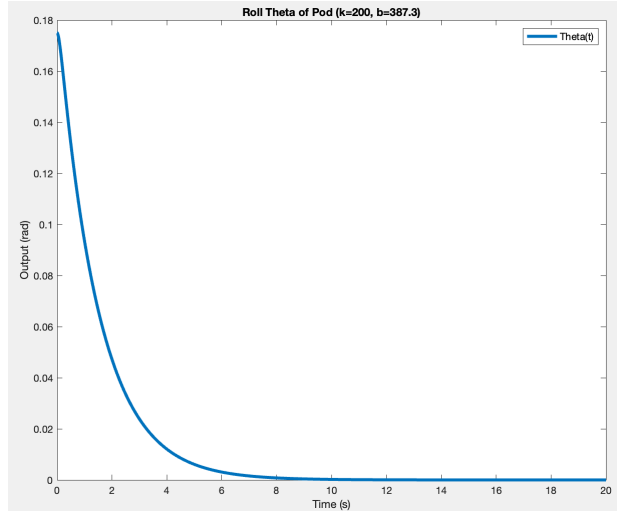


Figure 5: Matlab Simulation

## E Moment of Inertia

To approximate the moment of inertia of the pod-damper system, we set up a coordinate system approximately at the middle of the square box that will be representing the COM of the pod. From this we will use the moment of inertia tensor to find the numerical value of the moment of inertia about the yy axis.

$$I_{yy} = \int_{-w/2}^{w/2} \int_{-h/2}^{h/2} (x^2 + z^2) \sigma dz dx, \sigma = \frac{m}{wh} \quad (9)$$

This equation then simplifies to:

$$I_{yy} = \frac{m}{4} \left( \frac{w^2 + h^2}{3} + h^2 \right) \quad (10)$$

## G Previous Year Design

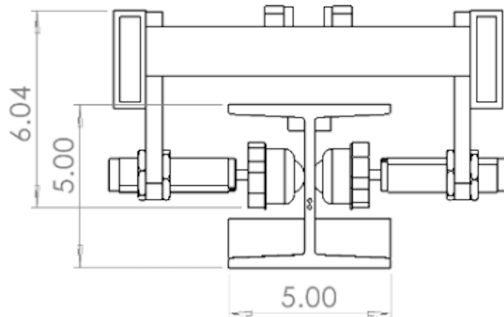


Figure 6: 2024 Horizontal Design

# 24-25 Hyperloop Global Electronic, Controls, and Communication System FDR

Aislinn Ennis

School of Electrical  
and Computer Engineering  
Cornell University  
ace68@cornell.edu

Shefali Awasthi

Bowers College of Computing  
and Information Science  
Cornell University  
sa652@cornell.edu

David Lilienfeld

Bowers College of Computing  
and Information Science  
Cornell University  
dal342@cornell.edu

Zarif Karim

School of Electrical  
and Computer Engineering  
Cornell University  
zk67@cornell.edu

29 March 2025

## 1 Abstract

The Electronics, Controls, and Communication subsystem is responsible for managing our pod's embedded software, ensuring accurate sensor data acquisition, and enabling seamless data communication between the pod and an external interface. This system is structured around two major components: the embedded system and the user interface. The embedded system manages all sensor configurations, handles power distribution, and transmits collected data to the onboard computer, where a state machine governs operational logic. The user interface, developed entirely in Python using the PyQt framework, establishes a two-way communication protocol between the onboard Raspberry Pi and a custom GUI. This interface provides real-time data visualization and control capabilities, forming the backbone of our automation strategy across other pod systems.

## 2 Design Specifications

### 2.1 Embedded Systems

Our embedded system centers on five key sensors: the MPU-6050 accelerometer, NTC 10K thermistors, a Maxbotix ultrasonic rangefinder, an Adafruit GPS unit, and a LIDAR sensor under evaluation for future implementation. During the research phase, we thoroughly reviewed datasheets to understand each sensor's power requirements, communication protocols, and pin configurations. We built test circuits on Arduino boards to validate sensor performance and compared hardware from different vendors based on reliability and integration cost. Testing included both short-term signal validation and long-term reliability trials.

The current sensor layout, detailed in Figures 2 and 3 of the Appendix, was developed to optimize data fidelity and maintenance accessibility. The Raspberry Pi is positioned in a location that minimizes thermal exposure and mechanical interference. The MPU-6050 is mounted centrally on a stable section of the pod to deliver accurate acceleration data with minimal distortion. Thermistors are strategically placed: one near the battery for safety monitoring and another close to heat-producing components. The ultrasonic sensor is bottom-mounted to measure pod elevation relative to the track, while



---

the LiDAR sensor, forward-facing, collects distance readings ahead of the pod. Each sensor is shielded from electromagnetic noise and is connected via modular connectors to ease replacement and system modifications.

### **2.1.1 Variable Frequency Drive**

The motor control system is based on a state machine implemented in C++. This logic evaluates real-time sensor inputs and transitions between operational states such as idle, acceleration, cruise, deceleration, and emergency. The Variable Frequency Drive (VFD) alters the motor's input frequency according to state transitions, adjusting the pod's speed accordingly. Functions are in place to process state logic and interface with sensor data, while placeholder routines represent future integration of sensor values. With each sensor integrated, the state machine is validated for accurate transitions.

The communication pipeline from the Raspberry Pi to the GUI operates using the ZCM middleware framework. Sensor values are published in a JSON format by the onboard system. The GUI parses these messages and updates display fields in real time. This system has been verified under varying Wi-Fi conditions, including Cornell's network and isolated routers, demonstrating robust performance without packet loss.

While sensor data is being processed and visualized successfully, reverse communication—sending commands from the GUI to the Pi—is currently under development. This functionality will allow the GUI to manually override states, such as triggering an emergency stop if automated detection fails.

To implement motor control, the Arduino receives serial commands from the Raspberry Pi. It maps characters '0' through '7' to one of eight binary-coded frequency profiles. Three digital output pins (D0, D1, D2) represent the binary selector lines. The Arduino adjusts pin states based on the input and sends a confirmation message back to the GUI, completing the command loop. This binary-based strategy ensures consistent, error-resistant VFD control.

## **2.2 User Interface**

### **2.2.1 Previous Design Features**

The user interface is designed as a multipage application with real-time monitoring and control tools for pod systems. The GUI offers dynamic graphing, profile selection, sensor monitoring, and emergency management. Each page of the interface is organized by function, such as live plotters for individual sensors, a dashboard overview, and FSM visualization.

The redesigned GUI supports user selection of predefined state profiles including Pre-Acceleration, Acceleration, Cruise, Deceleration, Stop, and Emergency. These profiles are color-coded for clarity. Sensor data is updated live, parsed from JSON packets, and rendered through PyQt's graphing tools. Users can view metrics for temperature, pressure, GPS coordinates, and accelerometer data, with adjustable time windows and graph settings.

In addition, the GUI includes a real-time FSM display that highlights the pod's current state and responds immediately to changes. A persistent emergency stop button is visible across all pages for safety. Battery metrics are aggregated on a dedicated page, summarizing voltage, current, and temperature across cells. The GUI also features a runtime timer and utilizes CSS styling for an intuitive and branded visual experience. The key features and important layout choices are consistent with our new design, but have been improved for ease of use and modularization.

### **2.2.2 Redesign**

The current year's work includes a full overhaul of our communication architecture. The updated GUI, now in development using Dash Plotly, will function both with and without internet connectivity, supporting Bluetooth data exchange with the pod. A new master relay system will control power and cooling subsystems, activated through both GUI and hardware interfaces. Emergency shutdown and system-wide overrides are core components of this update, enhancing reliability and control precision during test runs and competition scenarios.



---

## 3 Design Process and Research Timeline

### 3.1 Embedded Systems

Throughout Fall 2023, we developed our embedded systems by building on a state machine outline that defined pod states, key transitions, and required sensor data. We calculated expected values from sensors and used these as thresholds within the state logic to control pod behavior. The system evolved iteratively as each sensor was tested and integrated.

#### 3.1.1 Variable Frequency Drive

Early VFD control was hampered by poor documentation, prompting us to disassemble and reassemble the unit to understand its components and power pathways. After mapping its internal structure, we performed detailed testing on input pins and configuration parameters. Through this hands-on work, we established a reliable control strategy using three binary digital pins (D0–D2) to toggle among seven preset profiles. This approach replaced previous analog control methods, which were imprecise due to signal instability. Digital pin control proved more consistent and is being integrated into the GUI.

### 3.2 User Interface

The user interface has undergone continuous redesign since 2019 to match evolving pod requirements, budget constraints, and system complexity. The current framework supports subsystem data display and user control through a modular, scalable architecture.

## 4 Design Process Challenges

### 4.1 Embedded Systems

Budget limitations have historically restricted access to advanced sensors. While previous designs used short-range ultrasonic sensors, we've resumed development on more capable LiDAR alternatives due to a recent budget increase. Redundancy remains a core goal, and sensor additions are chosen to support fault tolerance.

#### 4.1.1 Variable Frequency Drive

Lack of public software libraries slowed development. Communication with the manufacturer was often required, introducing delays. Our initial attempts at analog control proved unreliable. Transitioning to digital pin-based selection allowed fast, stable frequency switching. This method avoids analog drift and enables consistent motor behavior by referencing predetermined profile values.

## 5 Future Design Iterations

Our next iteration emphasizes safety and robustness. We are integrating VFD control into a clean-slate electrical design and refining the state machine for edge case responsiveness. Future testing will evaluate behavior under nominal, emergency, and failure conditions using a dedicated test platform. Additional sensors will be added as funding permits, with a focus on resilience during malfunction scenarios.



---

## 6 Manufacturing Process

### 6.1 Embedded Systems

The VFD system required extensive validation at both the circuit and software levels. We verified proper voltage signals, observed motor response, and ensured that the control logic consistently matched user input. During integration, we confirmed that state transitions triggered appropriate motor actions without delay or electrical issues.

### 6.2 User Interface

The GUI was built as a modular system for easy debugging and expansion. Core functionality includes real-time sensor visualization, an emergency stop mechanism, and dynamic page loading. Key files are divided into logical components for application logic, layout design, and interaction handling. Installation involves setting up a virtual Python environment, installing dependencies, and launching the app via a local server.

## 7 Preliminary Timeline

### 7.1 Embedded Systems

Research and integration for the GPS and LiDAR systems are scheduled for early 2025, with testing and refinement continuing through the spring semester. Our testing is still in progress for this spring semester, finishing GPS module and full sensor system integration in the next couple of weeks.

### 7.2 User Interface

We completed a major structural redesign of the GUI during Fall 2024. This semester will focus on integrating our new GPS module and PWM controllers for levitation controls. In the future, there are plans to embed new features such as braking and cooling system interfaces into our GUI for complete pod control, once further testing is completed from our mechanical subteam.

## 8 Budget

### 8.1 Embedded Systems

This cycle's purchases include several Arduinos for parallel testing across subteams (50 USD), replacement cables (15 USD), a GPS module (25 USD), and a LiDAR sensor (estimated 50–200 USD based on ongoing selection for future iterations).

### 8.2 User Interface

The UI rework required no new expenses. The total projected cost for Spring 2025 is approximately 300 USD.

## 9 Analysis and Testing Process

To ensure the system's reliability and readiness for integration into the Hyperloop pod, a comprehensive testing methodology was followed across embedded systems, the user interface, and communication protocols. The goal of these procedures was not only to validate component functionality, but also to evaluate the resilience and responsiveness of the system under realistic and extreme conditions.



---

## 9.1 Embedded Systems

Testing began at the sensor level. Thermistors were subjected to controlled heating and cooling environments, and their outputs were cross-referenced against standard thermal curves. The accelerometer underwent repeated motion trials using known acceleration patterns to ensure low drift and high repeatability. GPS modules were tested both indoors and outdoors to evaluate signal acquisition times and location accuracy. The ultrasonic sensor was tested across different mounting heights and surfaces, and the results were analyzed for signal reliability and resolution.

These sensor tests informed calibration efforts that refined the expected value ranges used in the state machine logic. To evaluate the state machine itself, we simulated sensor data inputs across various edge cases—including invalid, delayed, or contradictory signals. Each simulated state transition was logged and compared against expected outputs to verify that state progression aligned with design requirements.

## 9.2 User Interface

The GUI was subjected to performance benchmarking under both standard and stress-test conditions. High-frequency data streams were simulated to emulate real-time operation during a pod run, and we evaluated graph rendering latency and packet parsing time. Visual update delays were kept within 200 ms, which we deemed acceptable for live monitoring.

User interactions such as triggering emergency states, switching between profiles, and resetting plots were tested across multiple operating systems and browsers to ensure consistent behavior. Additionally, the GUI's FSM mirror was checked for synchronization accuracy with the Raspberry Pi's on-board FSM. We also evaluated the GUI's handling of malformed or missing JSON packets to ensure the application degraded gracefully without crashing.

## 9.3 Variable Frequency Drive (VFD)

For the VFD subsystem, we tested both the software and physical circuit. Each of the eight profile selection inputs ('0' to '7') was sent via serial commands, and the Arduino's digital pins were monitored using a multimeter and oscilloscope to verify that the correct binary pattern was applied. Voltage and current surges during transitions were recorded and compared to expected VFD behavior.

We also examined response times for profile changes under load by simulating various speed scenarios. This included toggling between high and low speeds and observing motor behavior to ensure mechanical smoothness and signal stability. Pin signal stability and Arduino confirmation messages were verified for every case.

## 9.4 Safety Testing

To test the robustness of our safety architecture, we simulated multiple failure conditions, such as sensor disconnections, noisy inputs, and communication drops between the Pi and GUI. Emergency stop commands were issued through both software and hardware pathways to verify redundancy. Relay-based control systems, responsible for isolating subsystems during faults, were tested with actual current loads to ensure response under operational stresses.

Manual overrides for critical conditions, including overheating and unresponsive sensors, were activated and the pod's system behavior was observed through the GUI. Data from each of these tests—including activation delay, relay behavior, and system recovery—was logged for future analysis. All procedures were designed to expose weaknesses in the chain of communication between sensing, decision-making, and actuation layers.

Our documentation process involved maintaining test logs, timestamped error reports, visual dashboards, and performance metrics in team-accessible platforms like Confluence. These records serve as both validation artifacts and references for future design iterations.

# 10 Appendix

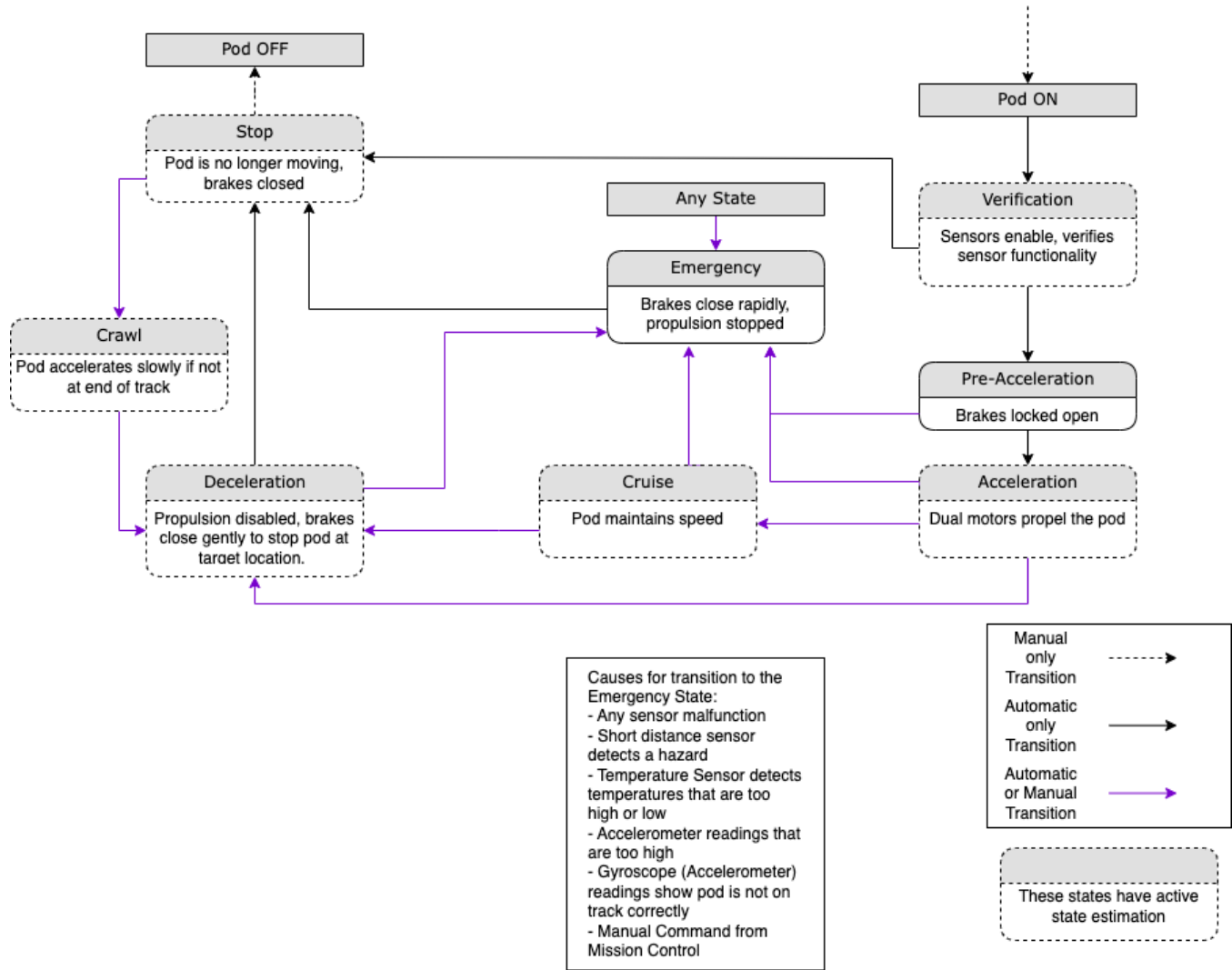


Figure 1: Finite State Machine

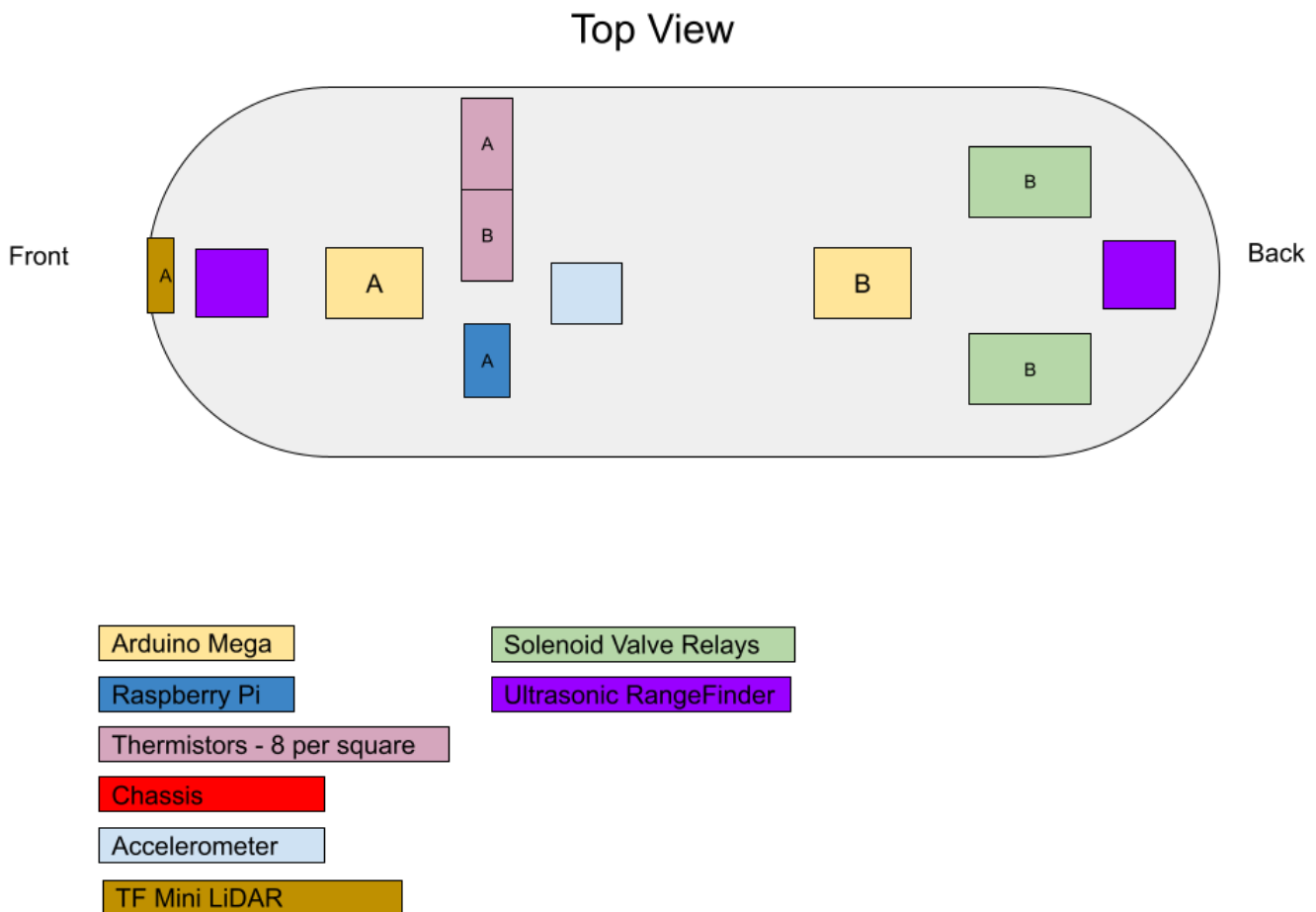


Figure 2: Sensor Layout (Top View)



## Side View

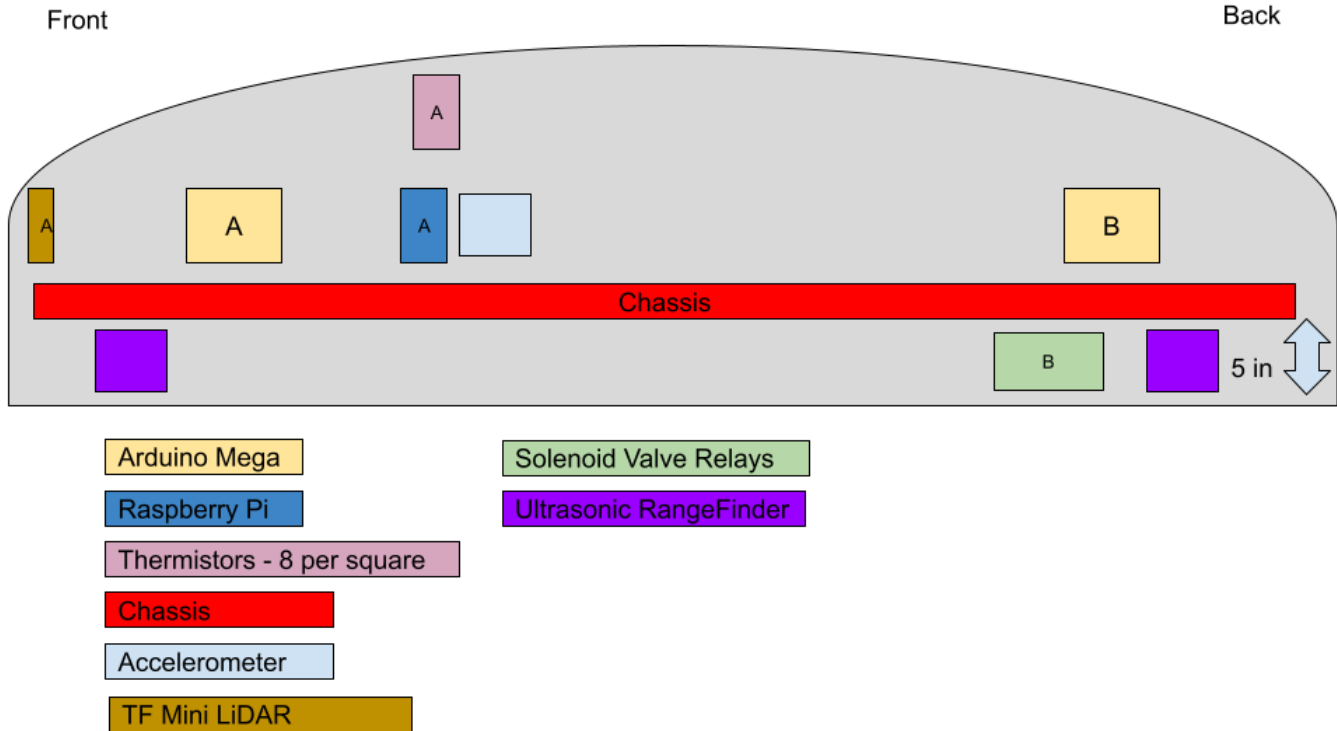


Figure 3: Sensor Layout (Side View)

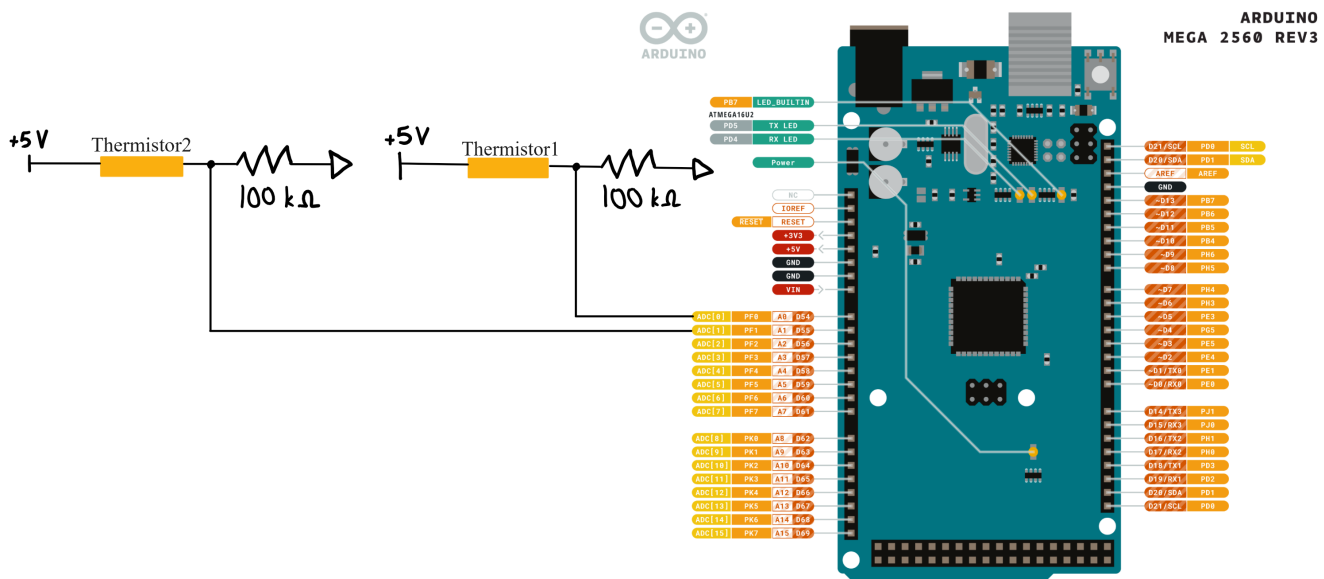


Figure 4: Thermistor Test Circuit

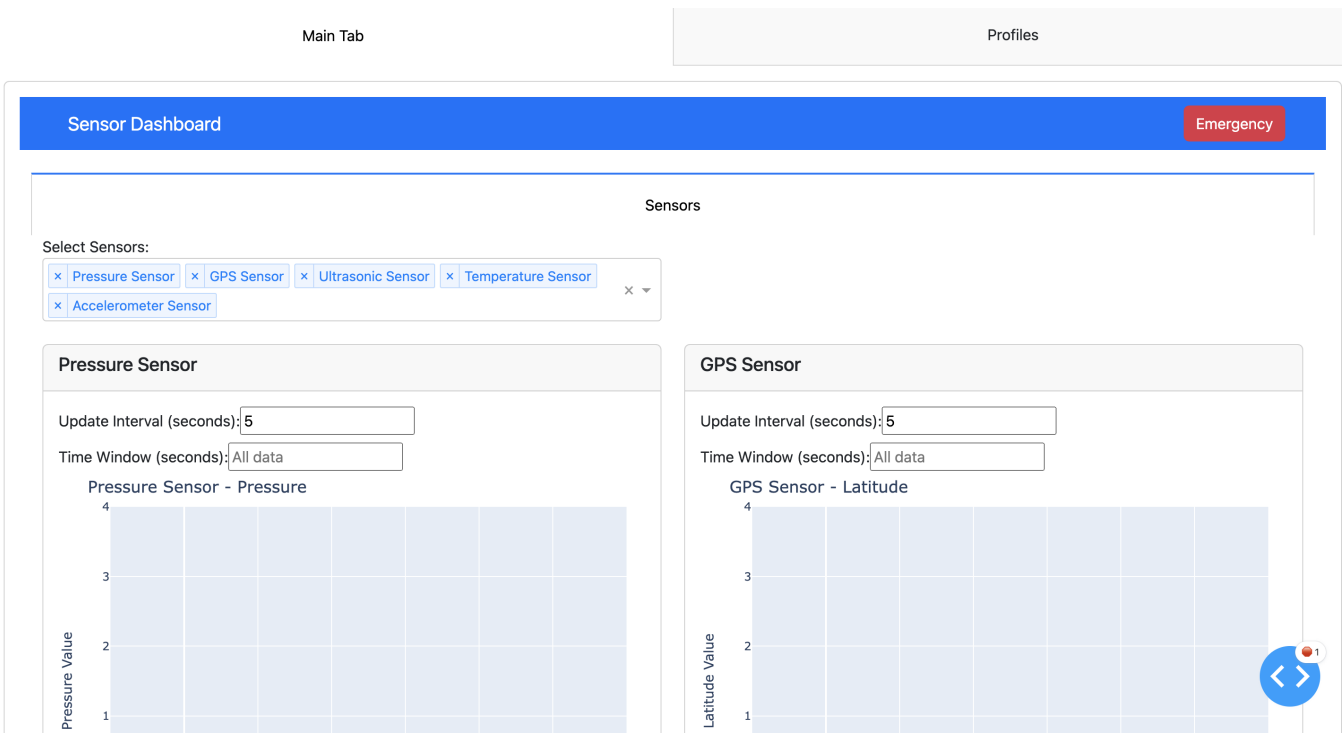
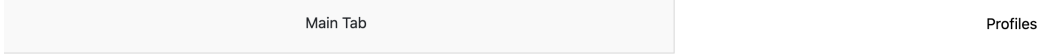


Figure 5: Graphical User Interface Design



### Select Profile

- Pre Acceleration
- Acceleration
- Cruise
- Deacceleration
- Crawl
- Stop
- Emergency



Figure 6: Graphical User Interface VFD Control System



Figure 8: Code Breakdown

The provided Arduino code is designed to control a Variable Frequency Drive (VFD) by selecting predefined frequency profiles based on serial input. Here's a detailed breakdown of how the code operates:

```
1 int D0 = 6; // Pin for D0
2 int D1 = 7; // Pin for D1
3 int D2 = 8; // Pin for D2
```

D0, D1, D2: These are digital output pins connected to the VFD. They are used to select one of eight possible frequency profiles (from Profile 0 to Profile 7) by representing a 3-bit binary number

```
1 void setup() {
2     // Set up D0, D1, and D2 pins as outputs
3     pinMode(D0, OUTPUT);
4     pinMode(D1, OUTPUT);
5     pinMode(D2, OUTPUT);
6
7     // Start serial communication
8     Serial.begin(9600);
9 }
```

pinMode(D0, OUTPUT); pinMode(D1, OUTPUT); pinMode(D2, OUTPUT); Configures the three digital pins as outputs to send signals to the VFD.

Serial.begin(9600); Initializes serial communication at a baud rate of 9600 bits per second. This allows the Arduino to receive commands from a connected computer or another serial device.

```
1 void loop() {
2     if (Serial.available() > 0) {
3         char c = Serial.read();
4
5         if (c == '0') { // Profile 1 (10 Hz)
6             digitalWrite(D0, LOW);
7             digitalWrite(D1, LOW);
8             digitalWrite(D2, LOW);
9             Serial.println("Profile 0: Knob on the VFD");
10        }
11        else if (c == '1') { // Profile 1 (10 Hz)
12            digitalWrite(D0, HIGH);
13            digitalWrite(D1, LOW);
14            digitalWrite(D2, LOW);
15            Serial.println("Profile 1: 10 Hz");
16        }
17
18        ...
19
20        else if (c == '7') { // Profile 7 (70 Hz)
21            digitalWrite(D0, HIGH);
22            digitalWrite(D1, HIGH);
23            digitalWrite(D2, HIGH);
24            Serial.println("Profile 7: 70 Hz");
25        }
26    }
27 }
```



---

Serial.available() > 0: Checks if there is any incoming data in the serial buffer.

char c = Serial.read(); Reads the incoming byte (character) from the serial buffer.

Profile Selection: Depending on the received character ('0' to '7'), the code sets the states of D0, D1, and D2 to represent a 3-bit binary number corresponding to the desired frequency profile.

digitalWrite(D0, HIGH/LOW); digitalWrite(D1, HIGH/LOW); digitalWrite(D2, HIGH/LOW); Sets each pin to HIGH or LOW to form the binary representation of the selected profile.

Serial.println("Profile X: Y Hz"); Sends a confirmation message back over the serial connection indicating which profile has been selected.

# 24-25 Hyperloop Global Propulsion FDR

Nikita Dolgopolov  
Sibley School of MAE  
Cornell University  
nd287@cornell.edu

Anubhav Nigam  
Applied & Engineering Physics  
Cornell University  
adn38@cornell.edu

29 March 2025

## 1 Abstract

The use of linear induction motor for propulsion system of a Hyperloop pod is essential to the mission of the pod - long-distance travel with virtually zero friction. By virtue of magnetic levitation, any form of drive propulsion is eliminated, as contact with the track is zero, so a linear induction motor must be used in order to provide translational force to accelerate the pod.

## 2 Introduction

The benefits from the usage of a linear induction motor range from efficiency, better power-to-mass ratio, long distance travel capability, and easy manufacturing/assembly/maintenance. The main components of a linear induction motor are the primary and secondary, the **primary** being the magnetic core + windings that create a variable magnetic field that induces interfacing eddy currents in the **secondary**.

There are two general types of linear induction motors:

- **Single Sided LIM** - a LIM configuration in which a single primary and a single secondary is used.
- **Double Sided LIM** - a LIM configuration in which 2 primaries surround the secondary.

In either configuration, either the primary or secondary is fixed in order to induce translational motion in the other. For the purposes of our application, our primary is an already purchased Linear Induction Motor - iron core with copper windings mounted to the chassis of our pod, and our (fixed) secondary is the aluminum T6-6061 track provided by most student Hyperloop competitions. The performance of the LIM can additionally be improved by ferromagnetic backing of the paramagnetic aluminum track, which we are currently trying with development of our own track. The geometry of the I-beam track makes a double sided LIM configuration undesirable when considering space constraints imposed by other subsystems on our pod (particularly braking and guidance) and given the slanted flanges of the I-beam, so we intend to utilize a single-sided LIM. This year's propulsion system design builds upon the design that was made last year with primary improvements coming from the Power Systems side.

## 3 System Design Specifications

### 3.1 Functionality and Requirements

The dimensions of our system are primarily constrained by the size/weight limitations of our pod, since the LIM will be the most mass-concentrated part on the pod. System constraints include:

- **Full Pod System Mass Constraint:** 236 kg, to prevent track damage and allow for robust levitation
- **Dimensional Constraint:** Must fit in 12" horizontal chassis width, and 10" vertical pod height

The major constraint that played role in the LIM selection process is the power available on the pod. The battery pack design was fixed to provide up to 325VDC at up to 22A in a normal mode of operation - these values dictate the maximum power available to LIM and its drive - VFD. The 325VDC are fed into the VFD, which converts them to the 3-phase AC power for the LIM.

### 3.2 Equipment

Using the mechanical size and electrical supply constraints of our system, we were able to identify a manufacturer that could provide us a LIM that would meet our desired specifications. We are reusing a LIM bought 2 years ago. It is an adapted model of LMAC1607C23B60 from H2W Technologies, as shown in the table below.

Mechanical Dimensions		General Configurations	
<b>Height</b>	76mm	<b>Voltage</b>	230VAC
<b>Width</b>	178mm	<b>Current</b>	20A
<b>Length</b>	412mm	<b>Phase Input</b>	3-Phase
<b>Air Gap</b>	3.175mm		

The LIM is mounted inside the chassis at the height of 0.125in from the track via aluminum tubes and angle brackets. The mounting is designed for a safety factor of 10+ on stress, and the hand calculations were confirmed via FEA Ansys Structural Simulations.

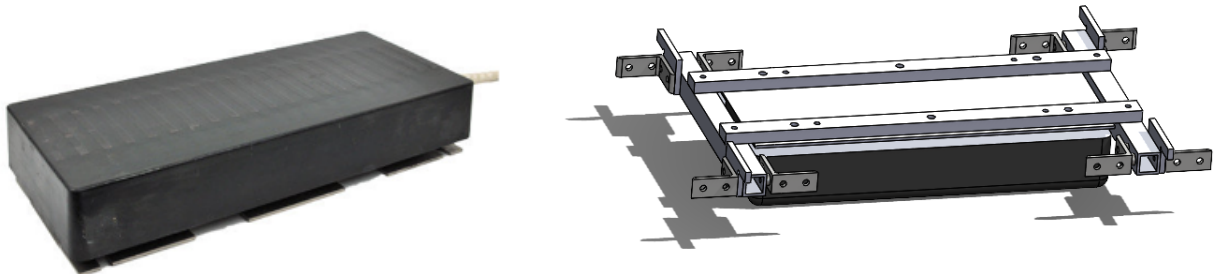


Figure 1: LIM and LIM Mounting

The drive was selected in accordance with the battery pack output values and the LIM input values: 325VDC at 22A to 3-phase 230VAC at 20A and a frequency of up to 120Hz. Such a VFD was found and purchased. A cheaper VFD was selected due to significant budget constraints and current lack of experience in working with high-voltage electronics: cheaper products allow us to experiment and have minimal losses in the case our design does not work out. After successfully testing the system with a 1HP VFD last year, 10HP version of it was purchased to be implemented this year. This is done to increase the thrust of the LIM 4-fold to make sure that the pod can start moving by itself.

This makes it that the main propulsion system components are the battery pack, the VFD, and the linear induction motor as described above.

### 3.3 Circuitry

The following circuit was designed to integrate the key elements of the propulsion system and to implement protection in case of failure of one or more devices, overcurrent protection, overheating protection, and manual start and stop switches. The whole circuit integrates the start, stop, EPO button, LIM's thermal switch and a buzzer to include manual switches and a latching circuit for the thermal switch. The VFD is connected to Battery pack via two DC lines through a fuse and a contactor (C). VFD feeds the LIM via 3-phase AC lines and 3 fuses for overcurrent protection. Both VFD and LIM are grounded to the battery pack negative. The contactor C is controlled via an additional contactor in a latching circuit and a 12V power supply. The thermal switch would cut off the power to the C contactor and effectively the LIM in the case LIM gets too hot: if the temperature inside the LIM reaches 120 degrees Celcius, the switch opens. The latching circuit ensures that, when the LIM cools back down and the switch closes, the power to contactor is not supplied - a manual intervention is required from the team engineer.

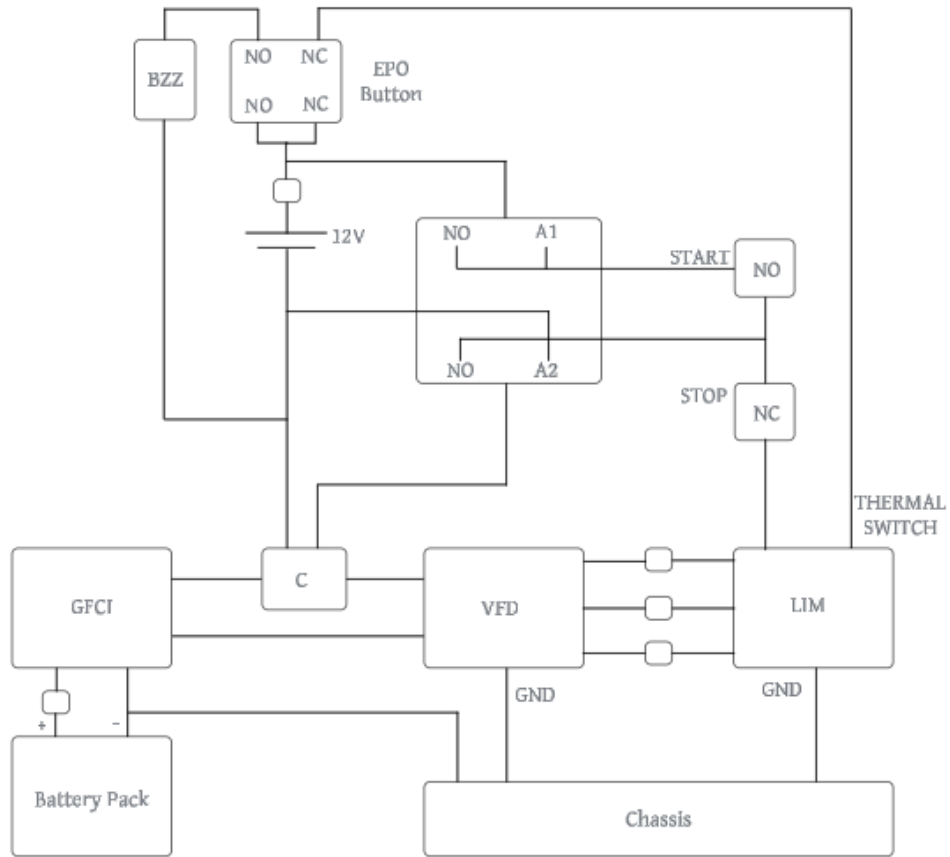


Figure 2: Electric Circuit

### 3.4 Hardware Mounting

The whole system is designed to be modular, so it is possible to assemble the whole unit and place it onto the chassis via the support hooks in four corners of the LIM mount. All electronics is mounted in the High Voltage Bay (Figure 3 in Appendix): a section with VFD, contactor, latching circuitry, and any other supporting electronics. The Circuitry is enclosed in steel enclosures, which protect it from the electromagnetic interferences from the LIM.



---

## 4 Testing

### 4.1 Goals

The primary values that are being tested are the speed and standstill thrust of the propulsion system. With speed, the primary concern is relating the frequency of input supplied from the VFD to the speed achieved by the LIM. Standstill thrust is relevant to the pod being able to start moving from a stationary state.

### 4.2 Test Rigs

The speed of the system is tested with a flywheel (Appendix E) - the LIM is mounted vertically facing flywheel such that there is an airgap of 1/8" between the LIM and the flywheel. This airgap emulates the actual distance between the LIM and the track in practice. The flywheel has multiple black markings on the edges, and there is a QTI sensor which is able to identify when these markings pass by. This information is used to calculate the speed of the flywheel.

Thrust is measured with a static I-Beam (Appendix E). The LIM is mounted above the I-Beam such that there is an airgap, and the I-Beam is mounted on linear rails such that it has 1 degree of freedom. There is a load cell in contact with end of the I-Beam, so the load cell can be used to measure the static thrust force of the LIM when the I-beam is pushed into it.

## 5 Project Costs

Below are presented approximate additional costs incurred this year on top of last years' progress, so expensive items like LIM(5000 USD) are not presented.

System		Testing	
Mounting	0 USD	Thrust Test Rig	500 USD
Electrical	150 USD	Flywheel Test Rig	350 USD

## 6 System Readiness Level

The designs from last year are manufactured. The machining of metal parts of the system has been completed, and the 3D printed parts for cooling system have been printed (Appendix B, Figures 6 and 7). The cooling system prototypes had been made to ensure fitting of all components and sufficiently good performance under higher temperature - affordable pumps used in the design may underperform at higher temperatures. Current work lies in developing and conducting safe LIM testing procedures for characterization. This has likely been the most complex part of the project, as it is important to ensure complete safety of our team members when working with such high voltages as 320V. Consequently, we are currently being consulted by the college safety engineers to ensure that a set of very specific guidelines is created for pod testing and operation.

Next steps also include developing a controller for the linear induction motor. It will utilize a DQ/ABC transform and a PID controller on the voltage - it will be fed into the VFD via a digital input to set the voltage and frequency (which are coupled). Before the controller is tuned, the dynamics of the pod needs to be characterized along with the magnetic circuit of the LIM. The magnetic circuit is depicted in Appendix C. Research is currently being conducted for determining the outputs of the LIM - the goal is to characterize thrust and speed of the system given the inputs in the form of frequency and voltage and given the system parameters in geometry and material properties.

## 7 Timeline

### 1. Sep 2024 - Dec 2024: Characterization Test Design

Development of the procedures for effectively and quickly characterizing the magnetic circuit of the LIM.

### 2. Nov 2025 - Mar 2025: Test Rig Design and Build

We were designing and manufacturing the upgraded Flywheel test rig and the Thrust test rig.



---

**3. (*PROJECTED*) Mar 2025 - Apr 2025: Testing**

The LIM will be characterized using both test rigs, and dynamical relationships will be numerically derived from the results of these tests.

**4. (*PROJECTED*) Apr 2025 - May 2025: Controls Test and Final Assembly**

We will test the control system of the whole pod and assemble it for track testing.

## 8 Conclusion

The process of designing the complete propulsion system has been quite challenging due to current inexperience with the process of designing such systems. It had proved to be difficult to find certain electrical components that fit the desired characteristics at the affordable price. Nonetheless, we were able to implement the propulsion system last year. The characterization testing of the LIM will be completed in March and the pod will be ready for competition in May.

In the next iterations, it would be helpful to investigate more expensive yet powerful cooling solutions as well as industrial inverters from more reliable manufacturers. However, this may not be necessary if the VFD performs as described. There are also aspirations of building our own Linear Induction Motor to suit our specific goals in 2-3 years.

## A Appendix A

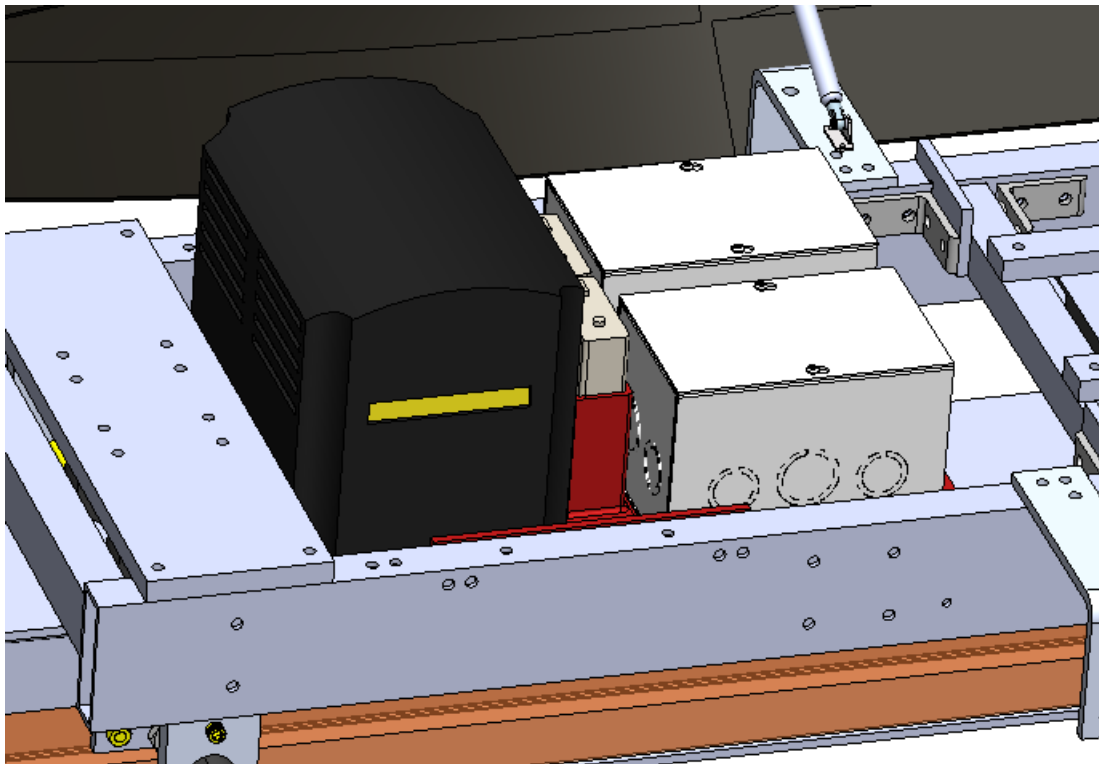


Figure 3: Electric Bay

## B Appendix B

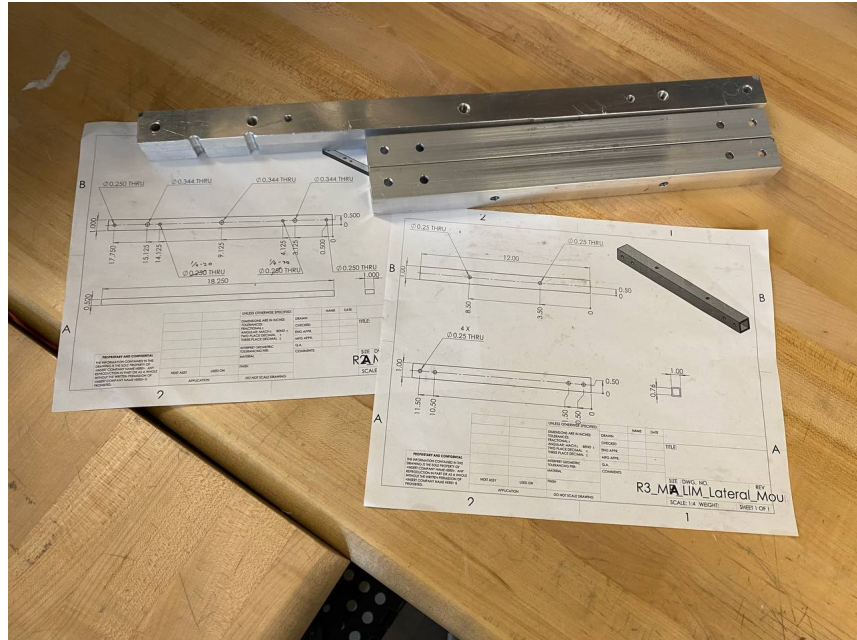


Figure 4: Machined Parts

## C Appendix C

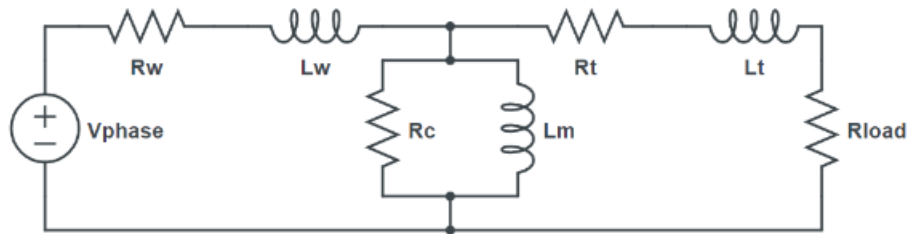


Figure 5: LIM Magnetic Circuit

$R_c$  - resistance of the core,  $L_m$  - magnetizing inductance,  $R_w$  and  $L_w$  - resistance and reactance of the windings,  $R_t$  and  $L_t$  - resistance and reactance of the track,  $R_{load}$  - mechanical load. The procedure for determination of their values is not covered in this paper.

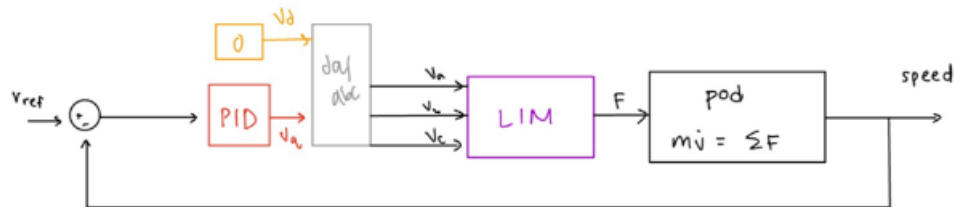


Figure 6: LIM Control Circuit Diagram

## D Appendix D

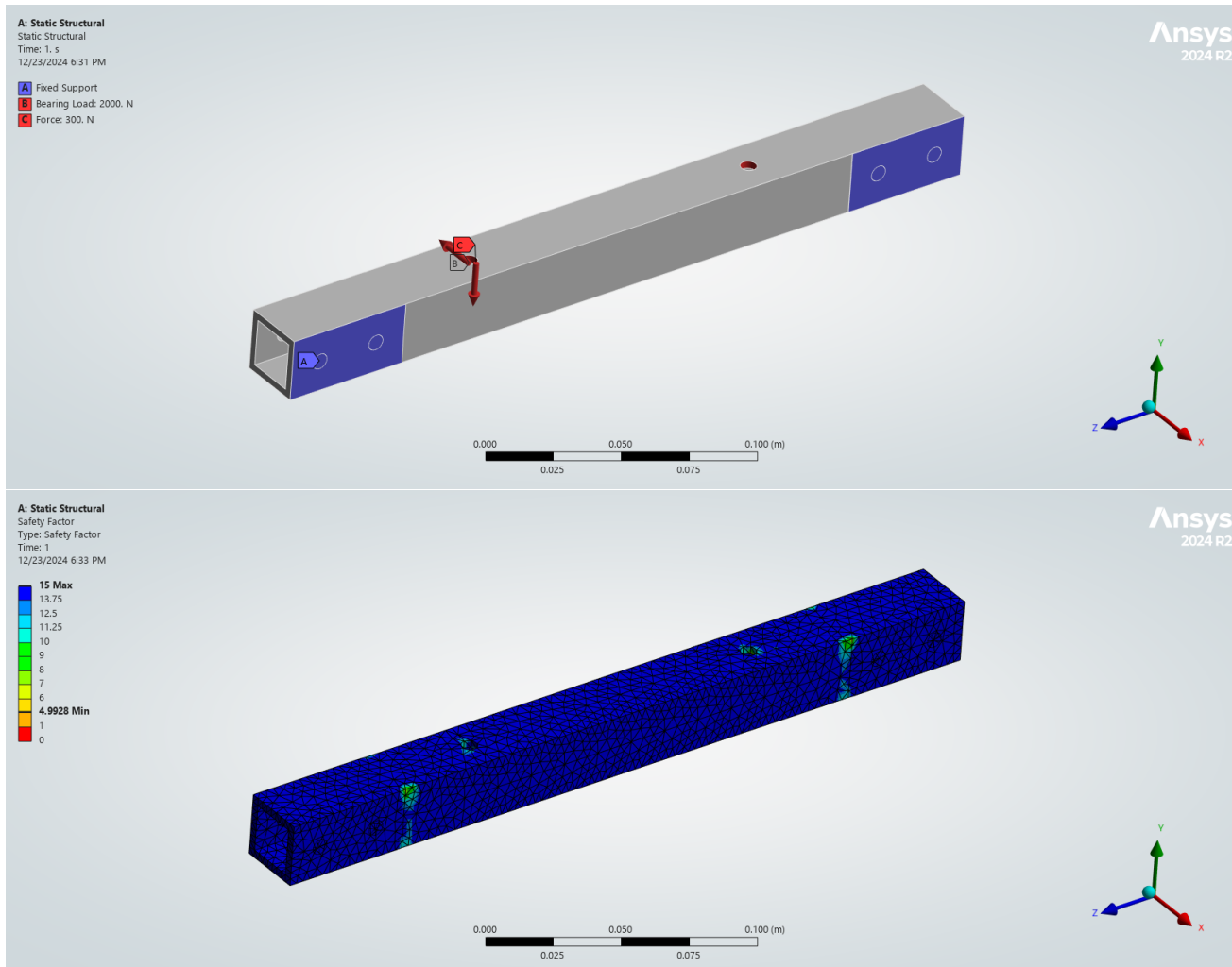


Figure 7: LIM Mount Ansys

## E Appendix E

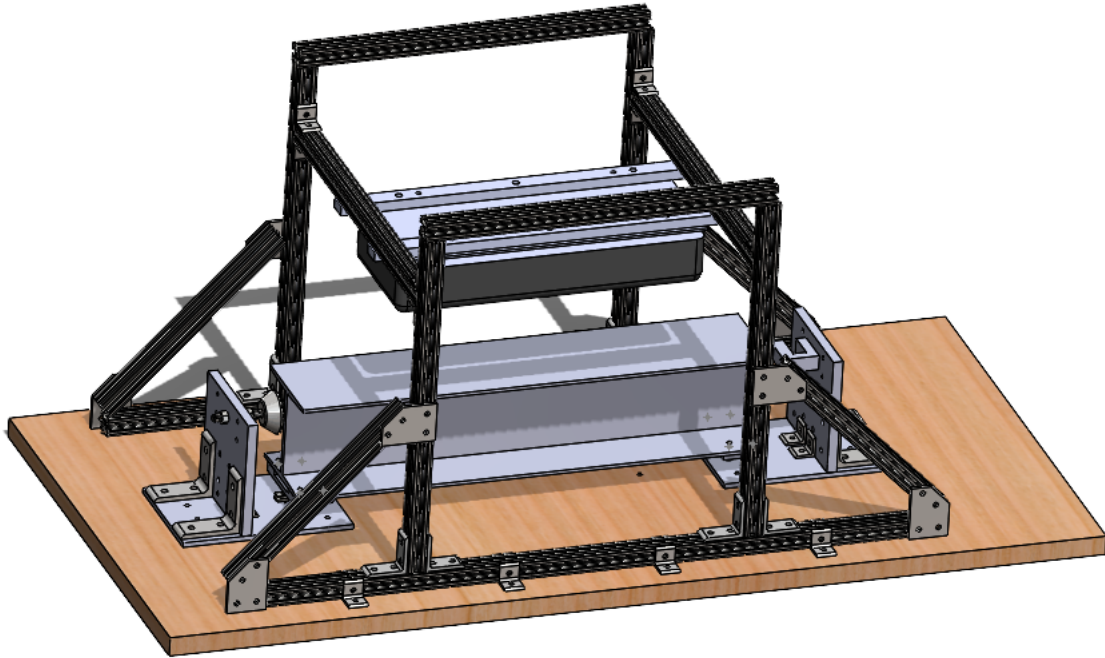


Figure 8: Thrust Test Rig

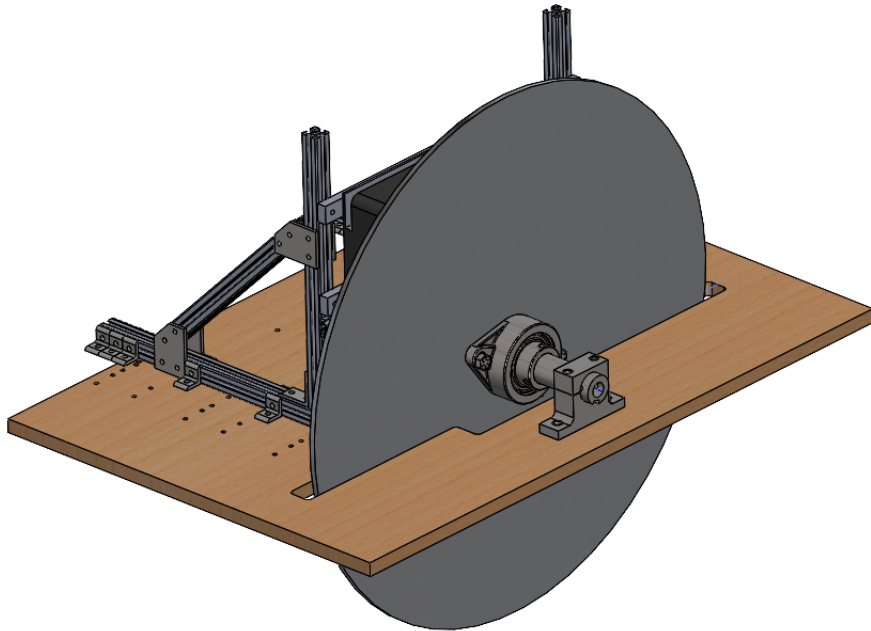


Figure 9: Flywheel Test Rig

# 24-25 Hyperloop Global Levitation FDR Paper

Riya Guttigoli  
Sibley School of MAE  
Cornell University  
rag323@cornell.edu

Eliza Phua  
Sibley School of MAE  
Cornell University  
ep555@cornell.edu

Alice Park  
Sibley School of MAE  
Cornell University  
sp2577@cornell.edu

29 March 2025

## 1 Abstract

The use of magnetic levitation (maglev) for a Hyperloop pod is essential to maintaining the transportation's novelty. Employing both static and dynamic levitation, the pod can travel with zero friction, allowing for high-speed travel. This proposal outlines the requirements of designing a maglev system for student competition and our team's research and system design.

## 2 Introduction

The goal of a maglev system is to levitate the pod above the track while the pod is both stationary and moving. This levitation prevents the entirety of the pod from being in contact with the track, resulting in zero friction. Zero friction allows for higher speeds and considerably increases motor efficiency and pod travel distance capabilities.

This year we are creating a miniature pod for the sole purpose of showcasing levitation on a modified track. Our team is using an aluminum wide flange track, and we are attaching ferromagnetic plates (reaction rails) to this track. The goal of our system is to have four modified transformers that act as electromagnets to attract these ferromagnetic plates while maintaining a small air gap.

## 3 System Design Specifications

Our team has chosen to modify transformers to act as electromagnets for our maglev system. This will allow us to take an existing transformer and utilize its limb and core, without having to wrap our own coils. The magnetic field lines for our modified transformers can be approximated by those in Figure (1). Our designs were heavily limited due to our design constraints, which came in the form of the 6061 T6 Aluminum I-beam track on which our pod is operating. In order to incorporate a ferromagnetic material into the track we are bolting a carbon steel plate to both sides of the I-beam flange in order to attract a ferromagnetic material. For this to work we are using a larger wide flanged I-beam.

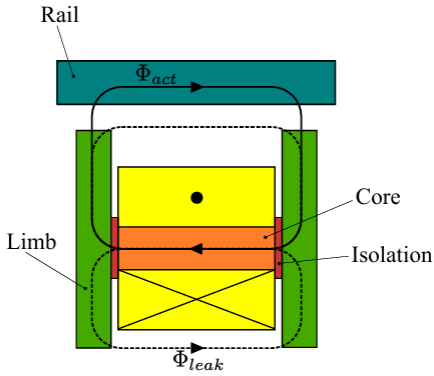


Figure 1: Magnetic flux path of transformer

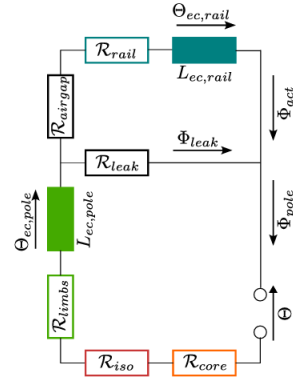


Figure 2: Magnetic Circuit

### 3.1 Functionality and Requirements

In order for our system to work, it must generate an electromagnetic force equal to that of the minipod's mass; this mass will be set around 15 kg. Because our system is an EMS system, it is considerably very unstable. If our electromagnets produce either too much or too little force, the pod will hit the track. In order for the levitation height to be maintained, the minipod must employ active control to read levitation height and vary supply voltage within a feedback loop.

### 3.2 Governing Principles

To determine the force that our electromagnets will generate we can model our system as a magnetic circuit. The magnetic circuit above (Figure 2) originates from a paper produced by TUM Hyperloop, and is titled, "Modeling of Coupled Electric and Magnetic Circuits in Electromagnetic Suspension Vehicles." We wish to solve for the acting flux to determine the force produced by each electromagnet. This force is expressed as:

$$F(t) = \frac{1}{2} \frac{\Phi_{act}^2}{A_{airgap} \mu_0} \quad (1)$$

In this equation,  $\Phi_{act}$  is the magnetic flux that passes through our reaction rails,  $A_{airgap}$  is the airgap area between the limb and rails, and  $\mu_0$  is the permeability of free space. To solve for the acting flux, you can apply Hopkinson's law to the magnetic circuit to equate the magnetic reluctances  $A_{mag}$  and magnetic fluxes  $\Phi$ , to the supply voltage induced electromagnetic forces  $\Theta$ . This gives the following system of two equations:

$$A_{mag} \Phi = \Theta - \Theta_{ec} \quad (2)$$

Each elements magnetic reluctance can be expressed by equation (9), which is found in the appendix. This equation is dependent on the materials relative permeability  $\mu_r$  which is not constant. To account for the variability in a materials permeability we must create  $B - H$  curves to find the permeability as a function of both magnetic flux  $B$ , and magnetic field strength  $H$ .

### 3.3 B – H Curve Testing

The  $B - H$  curve for a material shows the relationship between magnetic flux density and magnetic field intensity, crucial for understanding how a material's flux density saturates at high supply voltages. To determine this curve, we tested off-the-shelf transformers by supplying current through the primary

winding and measuring the voltage of the secondary winding. The primary current relates to magnetic field intensity through:

$$H(t) = \frac{N_{main} i_{main}(t)}{l_{core}} \quad (3)$$

where  $N_{main}$  is the primary winding turns,  $l_{core}$  is the magnetic path length, and  $i_{main}$  is the current through the primary. The secondary, or sense winding, measures magnetic flux density. The induced voltage,  $v_{sense}(t)$ , in the secondary is used to calculate magnetic flux density,  $B$ , as:

$$B(t) = \frac{1}{A_{core} N_{sense}} \int v_{sense} dt \quad (4)$$

Testing setup included a variable transformer, off-the-shelf transformers, and an oscilloscope to measure primary current and secondary voltage. Our tests provided a high level understanding of a few OTS transformers, allowing us to visualize the magnetization behavior of possible electromagnets. A B-H curve of resultant data can be found in the appendix under figure 7.

### 3.4 Force Testing

Using the information acquired from  $B - H$  curve testing, we progressed to testing magnetic force values of a few select electromagnets. The levitation test rig comprised of a vertically translating I-beam positioned above a load cell, with steel plates underneath each flange. The exposed coil of each electromagnet was fastened at a fixed air gap below the I-beam's flange for each trial. Increasing current was supplied to the magnet's coil with a DC power supply to steadily change the magnetic force attracting the steel plate. As the I-beam was pulled downwards, force values from the load cell below were collected and analyzed for varying initial air gaps. An image of the test rig can be found in figure 8 of the Appendix.

The preliminary stage involved testing three transformers from different suppliers, each of varying core material, size, wire gauge, and winding count. One transformer of the three overtly proved to exert the greatest magnitude of magnetic force, with which we conducted 7 trials of current sweeps with air gaps of three to ten mm. These tests outlined the following relationship between force ( $F$ ), current ( $I$ ), and air gap ( $d$ ) for the transformer:

$$F = C * \frac{I^n}{d^m} = 0.1061 * \frac{I^{2.0264}}{d^{0.5416}} \quad (5)$$

Graphical visualizations of the force-distance data is displayed in figure 9 of the Appendix.

### 3.5 Controls Testing

The control system is meant to maintain the proper air gap for levitation found from our force testing by manipulating the current supplied to the transformers. To test its functionality, we designed a linear guide and rail system that vertically constrained the electromagnets with a distance sensor. Using the sensor readings and the input current, we created a feedback loop to continuously monitor the air gap and vary the current such that the gap remained within an ideal range.

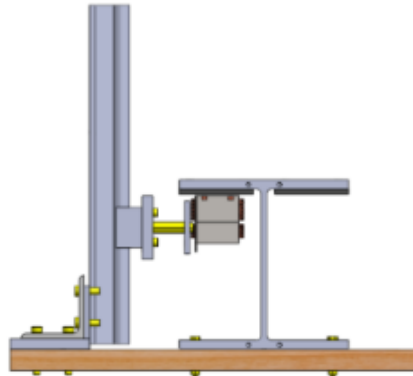


Figure 3: Lateral View of Controls Test Rig CAD

### 3.6 The Minipod

The goal of the minipod is to demonstrate the feasibility of magnetic levitation on a small scale. The pod, weighing approximately 15 kg, will levitate about 5 mm above the track. This is achieved using four modified transformers as electromagnets positioned below the flange of a wide-flanged I-beam. These transformers attract the ferromagnetic reaction rails on the track, creating a small air gap for levitation. Figure 10 in the appendix displays a schematic from TUM Hyperloop illustrating a similar levitation setup; however, we will use an I-beam track instead of an L-beam.

In order for levitation to be maintained, our team must establish a closed loop controls system that adjusts the imputed supply voltage to sustain a desired levitation height. The state space model for this closed loop controls system will be dependent on the  $B - H$  curves determined for testing, and will give our levitation height (air gap) as a function of supply voltage. The first or second order system graph can be seen in Figure 6. Further testing will determine what this air gap will be, but we estimate a value of around 3 – 7mm. In order to maintain this air gap will be have constant feedback read from an ultrasonic range sensor to determine what adjustments need to be made to our supply voltage.

### 3.7 Manufacturing

Manufacturing of the Minipod remains relatively simple. Following the conclusion of our testing procedures with confirmation of a viable transformers to satisfy magnetic force requirements, the Minipod frame will be assembled from 8020s to mount four transformers underneath the I-beam's flange. We currently estimate each transformer to fall within 100-200 dollar range, as we anticipate the core material will need to be close to pure iron. To harness the transformer's magnetic capabilities as electromagnets, we intend to slice each transformer's enclosure with a bandsaw to enhance exposure of the magnetic field to the steel rail. Caster wheels mounted to lateral plates will support the assembly sitting atop the I-beam when powered off. A visual of the Minipod prototype can be seen in Figure 11 of Appendix D.

## 4 System Readiness Level

At this point the Minipod assembly and magnet components are 90 percent finalized. Our active priority is testing controls with the chosen magnets using a test rig that measures air gap based on a dictated current input via a PWM controller. These results will give way to any necessary design changes before final Minipod assembly.



## 4.1 System Timeline

Magnetics subteam Fall semester progress:

Fall 2024	September	October	November	December
Magnetics Timeline	Meetings with TUM and research	Transformer ordering and $B - H$ Curve testing	Minipod schematic and assembly design	Controls system characterization

This is the projected Magnetics timeline for the remainder of the Spring semester, with the major focus being on the validation of a controls system to stabilize the levitation height for our minipod:

Spring 2025	January	February	March	April
Magnetics Timeline	Complete Manufacturing of I-beam components	Test magnets on I-beam test-rig	Change designs as needed, begin controls testing	Test full minipod w/ Controls

## 4.2 Future Design Iterations

Ideally, our model indicates that our system can realistically levitate a pod with some slight modifications to the electromagnet used during the tests. Possible results that would require modifications include the levitation force being too weak to lift the pod, the voltage requirements being too great, or the internal structure of the electromagnet not being strong enough to withstand the loading or heat generation requirements. If the minipod is able to statically levitate under its own weight, the goal is to have the system scaled up in future years, where eventually the entire pod can be levitating.

In the event that we conclude electromagnetic levitation with the current system is not feasible, we will most likely need to do a complete design overhaul, where we fully reconsider other possible levitation systems for the pod. Some other levitation systems include a spinning linear Halbach array, or turning a permanent magnetic into a controllable "on" "off" magnet, similar to how our magnetic braking system works.

## 5 Conclusion

The employment of a magnetic levitation system is imperative to maintain the novelty of Hyperloop technology. After unsuccessful implementation of such a system during last years design cycle we have scaled down our levitation goals in order to first prove viability. This will be accomplished with a miniature version of our pod, with the sole means of levitation. In order to aid in levitation we have opted to purchase and modify an I-beam track to make levitation more probable. In future years our team hopes to take the knowledge gained from the minipod to eventually scale up our levitation system such that full pod levitation is possible.

## A Magnetic Circuit Elements

The matrix for magnetic reluctances is:

$$A_{mag} = \begin{bmatrix} R_{pole} + R_{act} & R_{pole} \\ R_{pole} & R_{pole} + R_{leak} \end{bmatrix} \quad (6)$$

Where the pole reluctance can be expressed as a sum of material specific reluctances,

$$R_{pole} = R_{core} + R_{iso} + R_{limbs} \quad (7)$$

and the acting reluctance is

$$R_{act} = R_{airgap} + R_{rail}. \quad (8)$$

Each elements magnetic reluctance can be found through

$$R_{mag} = \frac{d}{\mu_0 \mu_r A} \quad (9)$$

where  $d$  is the length of the flux path,  $A$  is the cross sectional area of the element, and  $\mu_r$  is the materials relative permeability.

## B B – H Curve Testing

Our testing procedure requires us using a variable transformer to sweep across a range of supply voltages. Because of Ohm's Law, sweeping across supply voltages allows us to sweep across supply currents. This range of supply currents allows us to see both the linear, and non-linear (saturation) trends in our  $B - H$  curve. A typical saturation curve can be seen in Figure 7, with the linear portion occurring for small supply voltages only.

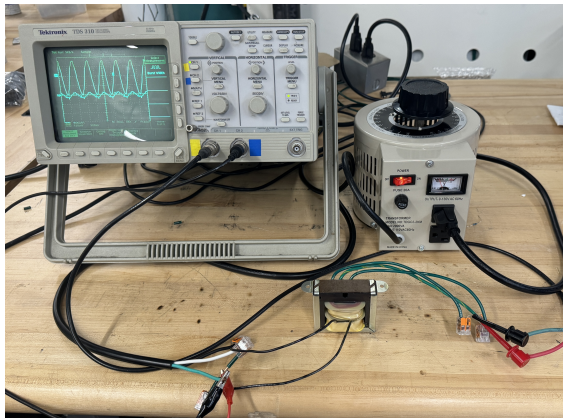


Figure 4: Transformer testing apparatus: Scope on the left, variable transformer on the right (power source), "magnet" towards the middle.

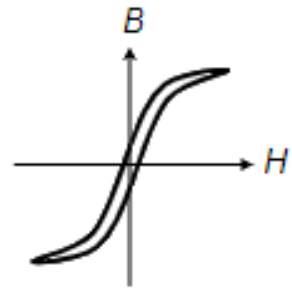


Figure 5: Curve with Saturation effects

Currently we have determined the step down voltage that our transformers supply, allowing us to determine the number of windings around each core by the turns ratio formula.

$$\frac{V_1}{V_2} = \frac{N_{turns,1}}{N_{turns,2}}. \quad (10)$$

## C Control System Specs

In order to ensure our levitation modules do not get too close to the reaction rails and stick to them we can treat our system as first order. We can also treat the system as second order with a maximum overshoot,  $M_0$ , equal to zero. This will ensure that our transformers do not get "too" close to the rails. A simple graph of this behavior is shown below:

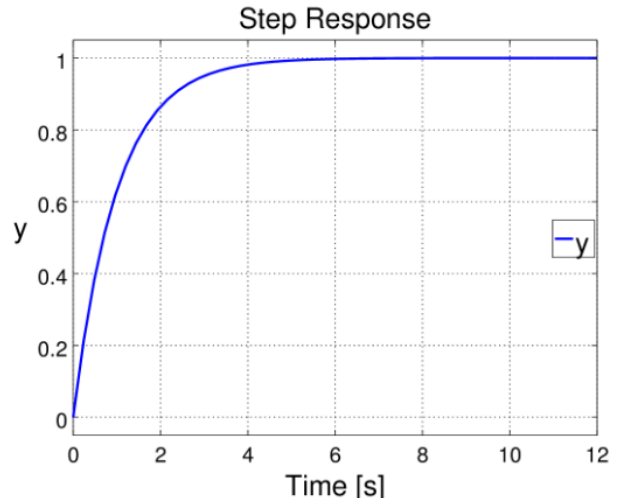


Figure 6: First Order System

The goal of the feedback loop will be to choose an air gap,  $R(s)$ , and continually approach this value. Our measurement output term,  $Y(s)$ , we come

from the constant reading of our current air gap from the ultrasonic range sensor. The error term,  $E(s)$ , that is read into our system will be the differ-

ence between  $Y(s)$  and  $R(s)$ . This error term will then dictate the magnitude of the control input  $U(s)$ .

## D Appendix Figures

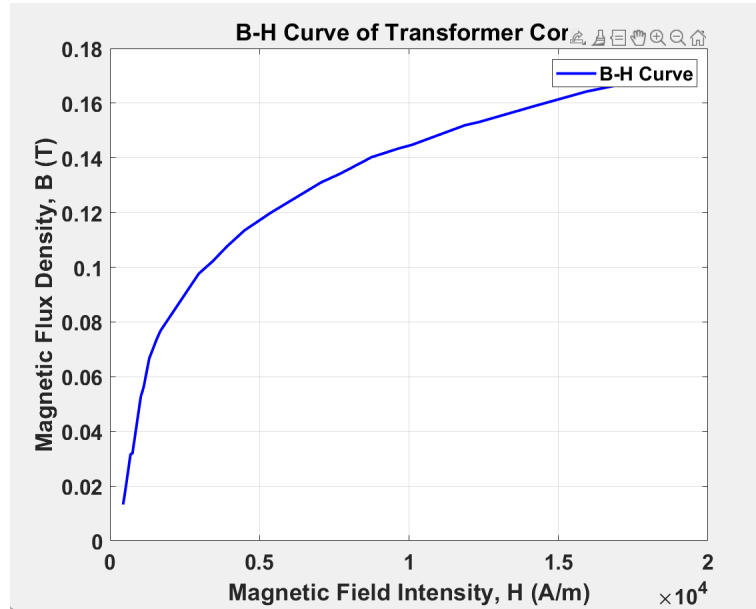


Figure 7: B-H Curve of Transformer

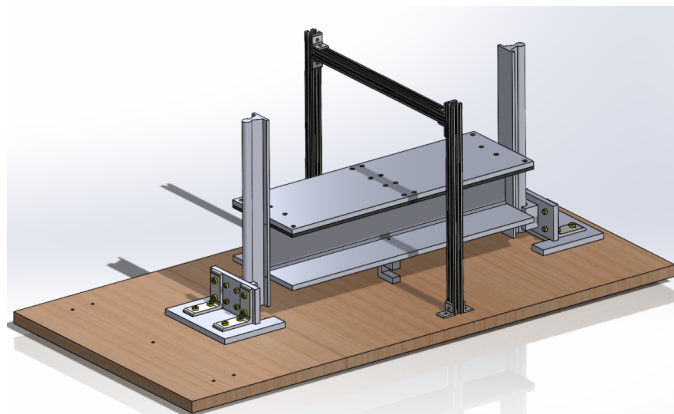


Figure 8: Transformer Levitation Test Rig

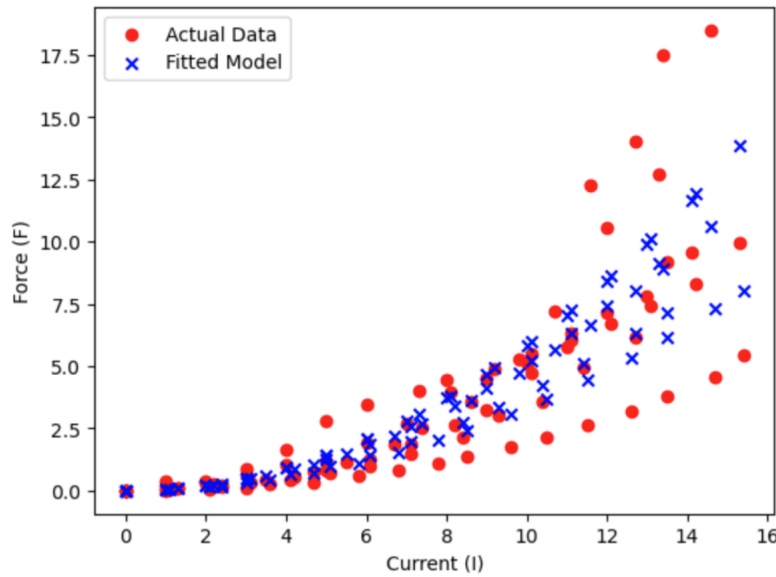


Figure 9: Electromagnet Current v Force Data

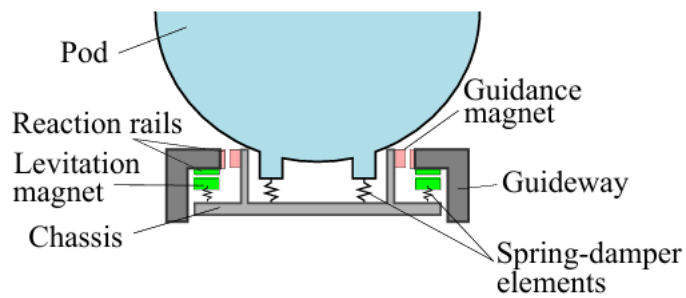


Figure 10: Cross Section of Hyperloop vehicle

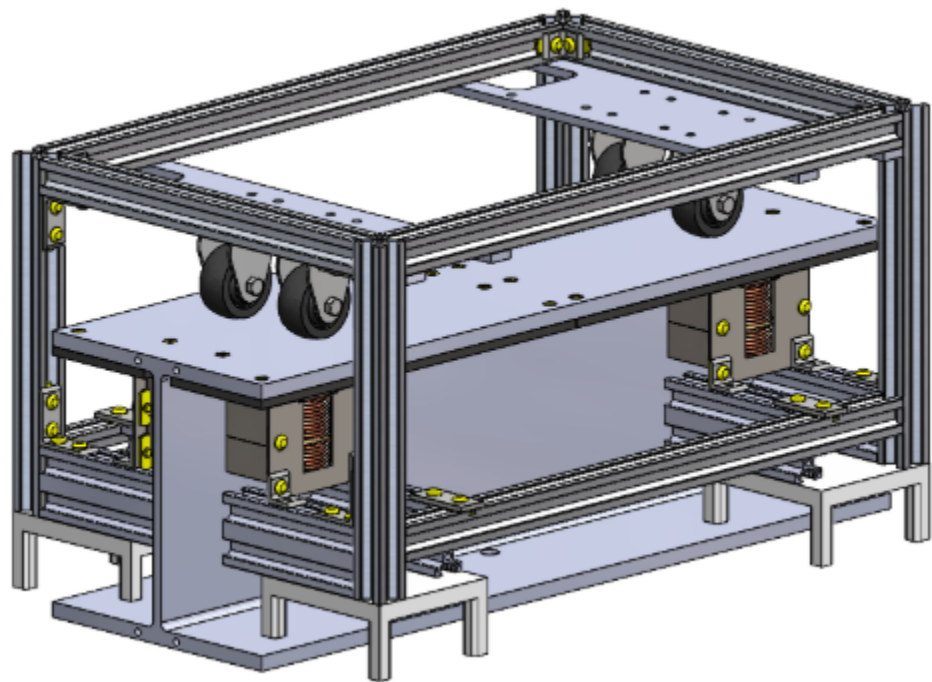


Figure 11: Isometric view of the minipod

# 24-25 Hyperloop Global Power Systems FDR

Max Trager  
Cornell University  
mt687@cornell.edu

Kirti Bagepalli  
Cornell University  
kb593@cornell.edu

Lalo Espanza  
Cornell University  
hle37@cornell.edu

Ivan Huang  
Cornell University  
qh229@cornell.edu

Tribeca Kao  
Cornell University  
ck795@cornell.edu

29 March 2025

## 1 Abstract

The Power Systems team is responsible providing and monitoring power to all other systems on the pod. Our team can be divided into two systems: high-voltage and low-voltage. The high-voltage system includes equipment that powers the linear induction motor (LIM), which consists of a high voltage power source, a DC to AC inverter, battery management system (BMS), and variable frequency drive (VFD). The low-voltage system includes equipment that powers everything else, such as low-power AC and DC power supplies. Overall, the primary goal of the Cornell Hyperloop Power Systems team is to meet the power specifications of mechanical and electrical components while taking proper safety precautions.

## 2 Design Specifications, Manufacturing, and Testing

### 2.1 System Requirements

The primary goal of the high-voltage system is to power the LIM, rated at three-phase 230 VAC, 105 Hz at 10 hp. Achieving this functionality requires a mechanism that converts a high power DC source into three-phase voltage.

### 2.2 Variable Frequency Drive

Our team decided to use an off-the shelf variable frequency drive to control the motor and achieve the desired three phase output. The VFD has a built-in inverter and variable output frequency from 0 to 400 Hz, rated at 10 hp and 230 VAC. Typically, VFD's take in 3 phase VAC, but it can also be powered by a DC source though the bus voltage with a rating of 325 VDC calculated using the relationship:

$$V_{bus} = \sqrt{2} \cdot V_{rms} \quad (1)$$

Additionally, as the output frequency of the VFD varies, this results in the variation of the output power and voltage. Typically in a VFD, the power and voltage relationship is linear from 0 to 60 Hz, where power is 0% at 0 Hz and 100% at 60 Hz. The power remains approximately constant from frequencies 60 Hz to 105 Hz, which is the desired frequency. The same pattern is followed for output voltage as well. See Figure 1 in the Appendix.



## 2.3 Safety Design

The design above accomplishes powering the linear induction motor; however, since this system is at such a high power, following safety standards is crucial.

### 2.3.1 High Voltage Connections

The connections between the battery pack and VFD as well as between the VFD and LIM must be properly rated. As our battery pack is operating at a maximum discharge current of 30 A, a 10 gauge, single-strand, solid copper wire is being used for our application. Our VFD has screw-clamp wire connections, thus we are using heat-shrink ring terminals to secure wires to the terminals of the VFD (both input from the battery pack and output to LIM). Wires are inserted into the ring terminal, and secured via heat shrinking. The ring terminals are then latched and secured onto the screw terminals of the VFD. Systems will be grounded to the main negative of the battery pack.

### 2.3.2 Fusing

We are also implementing fuses between the battery pack and VFD, as well as between VFD and LIM. For the prior, we will be using 30A fuses to prevent overcurrent to the VFD from the battery pack. This fusing between battery pack and VFD is a backup to the BMS, which also monitors for overcurrent. For the latter, between VFD and LIM, we will be using three 20A fuses, one for each phase of AC current. system.

### 2.3.3 Enclosures

To protect ourselves from electrical exposure and to ensure isolation between low and high voltage components, we will use a set of enclosures. These enclosures will be made of a non-conducting material, and will have screw-clamp wire holes. With the exception of the LIM and VFD (these systems are self contained), we will be enclosing all high powered and vital electrical components.

### 2.3.4 EPO Circuit

The high power LIM-VFD system must be monitored and controlled to ensure the safety of the pod and those around it. This is done by implementing an Emergency Power Off (EPO) circuit, which allows us to remotely start and stop the LIM. In a high level overview, our EPO circuit uses two switches, one turns the system on and one turns it off, and when the system is on a latching contactor is turned on, and power flows from the battery pack to the VFD-LIM. When the EPO circuit is turned off, then, the contactor disconnects and the VFD-LIM is no longer powered. The EPO circuit is controlled remotely via a Bluetooth module that changes the state of an Arduino. Additionally, the EPO takes information from the LIM, and if the LIM reaches a temperature above its nominal temperature, the EPO circuit will turn off and the LIM will no receive any power. See Figure 2 for the EPO schematic.

This circuit has been implemented on a PCB. This reduces the size of the electrical system while enhancing the stability of the connections between the EPO circuit, Arduino, and Bluetooth communication module because they are all integrated into a single board. See Figures 3 and 4 for the PCB schematic and a picture of the physical PCB board.

To implement this EPO circuitry, we used four relay modules to represent the two remote switches and a latching contactor. Each relay module is rated for 10A at 30VDC. The two remote switching relays are powered by 5V VCC from the Arduino, while the latching contactor relays are powered by a 12V supply. Pins from the Arduino function as start and stop controls. When the start signal is set to High and the stop signal is set to Low, a 12V signal is sent to the latching contactor relay, enabling it to connect and latch. This system remains in this state until the stop switch is set to High or the Bluethooth module, which disconnects the contactor and the LIM is no longer powered.



---

## 2.4 Battery Pack

### 2.4.1 Overview of Materials and Process

As mentioned before, the battery pack consists of 100 A123 LiFePO<sub>4</sub> 26650 cells connected in series and will be divided into three modules of 32, 34, and 34 cells connected together through copper busbars. See Table 1 for Battery Cell Specifications. More specifically, it will be arranged such that there are two columns of 16, 17 and 17 cells for the 32, 34, and 34 cell modules, respectively. Given that all cells of the battery pack are connected in series, battery cells of each module will be arranged such that one face of the pack consists of adjacent cells with alternating positive and negative terminals. This configuration ensures that the positive terminal of one battery cell will be connected to the negative terminal of an adjacent cell through spot-welding. For the specific strip material that will be used to spot-weld each cell together, we decided through testing of different copper-nickel thicknesses and ease in establishing strip-cell bonds that 0.15 mm pure nickel stacked with 0.15 mm copper strips were the most viable option. To prevent the short circuiting of individual cells during and after pack assembly, pieces of mica paper will be inserted between and on the tops of each battery cell. See Figure 6 for an illustration of the battery pack diagram.

### 2.4.2 Preparation for Spot Welding

Initial steps that must be taken prior to assembling the battery pack involves testing that each LiFePO<sub>4</sub> 26650 cell has the same nominal voltage. This will simply be achieved through probing the positive and negative terminals of each battery cell using a multimeter, making sure that each cell displays a voltage of 3.25 V, and discharging certain cells to a balanced voltage if needed. Such tests are done to prevent the BMS from having to balance the pack through application of resistance and removal of extra charge, which could potentially take up a significant portion of runtime.

### 2.4.3 Spot Welding Process

After testing the spot welding of different thicknesses of copper and nickel and the power settings of the spot welder, we settled on powering the spot welder to the 30 power setting for consistent connections. In order to maintain safety during the process, we will ensure the use of safety goggles and spot welding gloves along with spot welding on the 1600 V insulation mat. In addition, we have broken up the spot welding of each of the three modules in order to maximize safety and protection of the battery modules during transportation. We have decided to spot weld the 34 cell modules first with smaller modules of 10-10-10-4, and similarly we will spot weld the 32 cell module first with smaller modules of 10-10-10-2. Then we will connect the smaller modules to have a total of three 34, 34, 32 cell modules to encompass our battery pack. Throughout the spot welding process we must ensure that there is consistency in the pressure while spot welding as over spot welding can cause corrosion issues and under spot welding can cause a loose connection interrupting the function of our entire battery pack.

### 2.4.4 Battery Pack Charging

Finding a suitable way to charge the Battery Pack was a significant challenge. To charge the battery pack, our team will connects the main positive and negative terminal of the battery module (10/12s) to a power supply with the max voltage set as the max voltage of the battery module. However, since every battery cells has slightly different chemistry makeup that create a small difference in full state of charge voltage. Cell voltage imbalance will happen and damage the battery module to prevent one cell being overly charged while other cells still require charging. One solution we tried is through purchasing an Orion battery management system(BMS), but it failed to operate, so we decided to build our own BMS for the battery pack module. The primary purpose of the BMS is to allow passive battery cell balancing to prevent cell voltage imbalance, our team came up with the following design after extensive research.



---

Figure 7 is a simplified schematic of the BMS. As we have chosen the 10/12 series battery cell modules, we will assign a BMS for each battery module and charge them individually. The BMS can be broken down to 3 parts, the cell balancing circuit, input voltage limiting circuit, and input current limiting circuit. Each BMS module will have 10/12 cell balancing circuit that will be connected to 12 individual cells in the module, dissipating input voltage when its corresponding cell voltage is detected as a full state of charge. The input voltage and current limiting circuit protects the battery from being distorted when the battery module is being charged with power source that provides high charging voltage and current than the module destinated voltage or current.

Currently, the schematic of the BMS is finished, and going through validation and testing. From now to competition, our team will validate the BMS functionality of cell passive balancing during charging on both individual cell, one 10/12 cells module, and multiple modules connected together. After the design is fully validated, our team will design a customized PCB for the BMS module for all battery pack module, then validate the functionality of the BMS PCB before putting the full battery pack with BMS on the train.

#### **2.4.5 Battery Backup Power**

To provide a backup to our battery pack system, we have also been developing a low-voltage car battery backup option. To accomplish this, we use a 240VAC inverter to turn the 12V DC output of a car battery into usable power for our VFD (which takes in 180-250 VAC, single phase). We are using a 12V, 300Ah LiFePO4 Deep Cycle battery, with 250A max discharge. With this system comes increased safety (as the pack operates at 12V, with a built-in, industrial BMS), but significantly increases the amount of current we need to handle from battery pack to inverter. At max output, the battery can run 250A to the inverter, so we are using heavy-duty 4/0 gauge copper cable between the car battery and inverter. This wire is rated to 400A under 50V in our operating conditions, which provides a significant safety/surge margin. With respect to testing, we have recently received materials, and have been able to confirm proper inverter output (240VAC) under no load. In the coming weeks, we will connect the inverter output to our VFD and LIM in order to perform thrust testing to get a sense of the electrical requirements of the system at varying frequencies.

#### **2.4.6 Safety Considerations**

In order to establish connections between each cell (and given the alternating configuration of each adjacent cell), it is unavoidable that each module must be flipped several times during the spot-welding process. The possibility of cells moving out of place and causing the metal strips to bend and short circuit certain cells whilst flipping the modules is a major concern in the assembly process. Certain considerations and steps taken to mitigate the chance of this happening include using spacers to give the module some stable structure, using large insulating surfaces to flip the entire module, and limiting the amount of cells per module, as the larger the module, the more potentially unstable it becomes.

Given that the battery pack is rated for 320 V and 20 to 22 A, there are also many safety precautions that must first be taken into account prior to assembly. As mentioned in the spot welding process, such measures include laying a high voltage insulated mat rated at 1600 V beneath the battery pack during and after spot-welding, along with wearing safety glasses, rubber gloves, and other protective insulating covering during the assembly process. If the battery pack must be left alone without supervision whilst in the middle of the spot-welding process, the pack must be kept either in a locked box or be covered completely with insulating material as to prevent people from accidentally coming into contact with this high voltage system.

After completion of the battery pack assembly, it is recommended that the enclosure walls be lined with self-extinguishing and insulating material such as mica epoxy or polycarbonate. The enclosure itself will be 3D printed to match the dimensions of the battery pack, and will leave only connections between the pack and other components such as the BMS exposed. Exposed cell tap harnesses and other wires must also be protected.



---

### 3 Design Process Moving Forward

#### 1. April 2025 - LIM and Magnetics Testing

We will test to see how the alternate power source effects the LIM's behaviour as we change the output frequency of the VFD. This will also allow us to test the behaviour of the VFD, and we can compare the data we collect to what we expect. Simultaneously, we will continue to develop our own BMS in the hopes of using our batteries to power the LIM. We will also help the mechanical team with their magnetics testing by ensuring proper procedures are taken to maintain safety.

#### 2. May 2025 - Finalizing On-Pod Circuitry

After testing all of the systems, we will work with the mechanical team to integrate all of the systems safely onto the pod so it is ready for competition. We will run final tests to ensure that everything is working as intended.

### 4 Design Process Challenges and Budget Constraints

This year Power Systems has faced great difficulty with working with our old BMS. We did a lot of research on how to use it and used many work sessions to look at the code and test the BMS, but it never worked properly. This challenge led us to the idea of developing our own BMS, which we are currently working on. Another challenge we faced is safely charting our battery pack modules, which we are hoping the BMS we build will help fix.

We did not have too many budget constraints this semester because we were fortunate enough to raise a sufficient amount of money at the beginning of the school year to allow us to purchase everything we needed and leave some over for unexpected expenses.

### 5 Future Design Iterations

The next iteration of our pod has various new features. Firstly, to power low-voltage AC components, we are planning to use a portable charger with a standard outlet. Additionally, the emphasis on safety components will be continued into the next iteration, which includes the introduction of a safety shut-off circuit and more contactors. Moreover, the last few iterations of the design included a battery pack, but this year we are most likely using the alternate power source discussed earlier. In future iterations, we will simultaneously continue to develop our own high power supply while also making the existing one more space and power efficient. Lastly, a suitable power supply system will need to be implemented for the mechanical team's magnetic levitation research project once that project comes to fruition. From initial mechanical testing, it will likely require lower DC voltage (30-40VDC) but much higher current (on the order of 20A), which cannot be powered by any of our current systems. This will require much research and safety testing.



## 6 Appendix

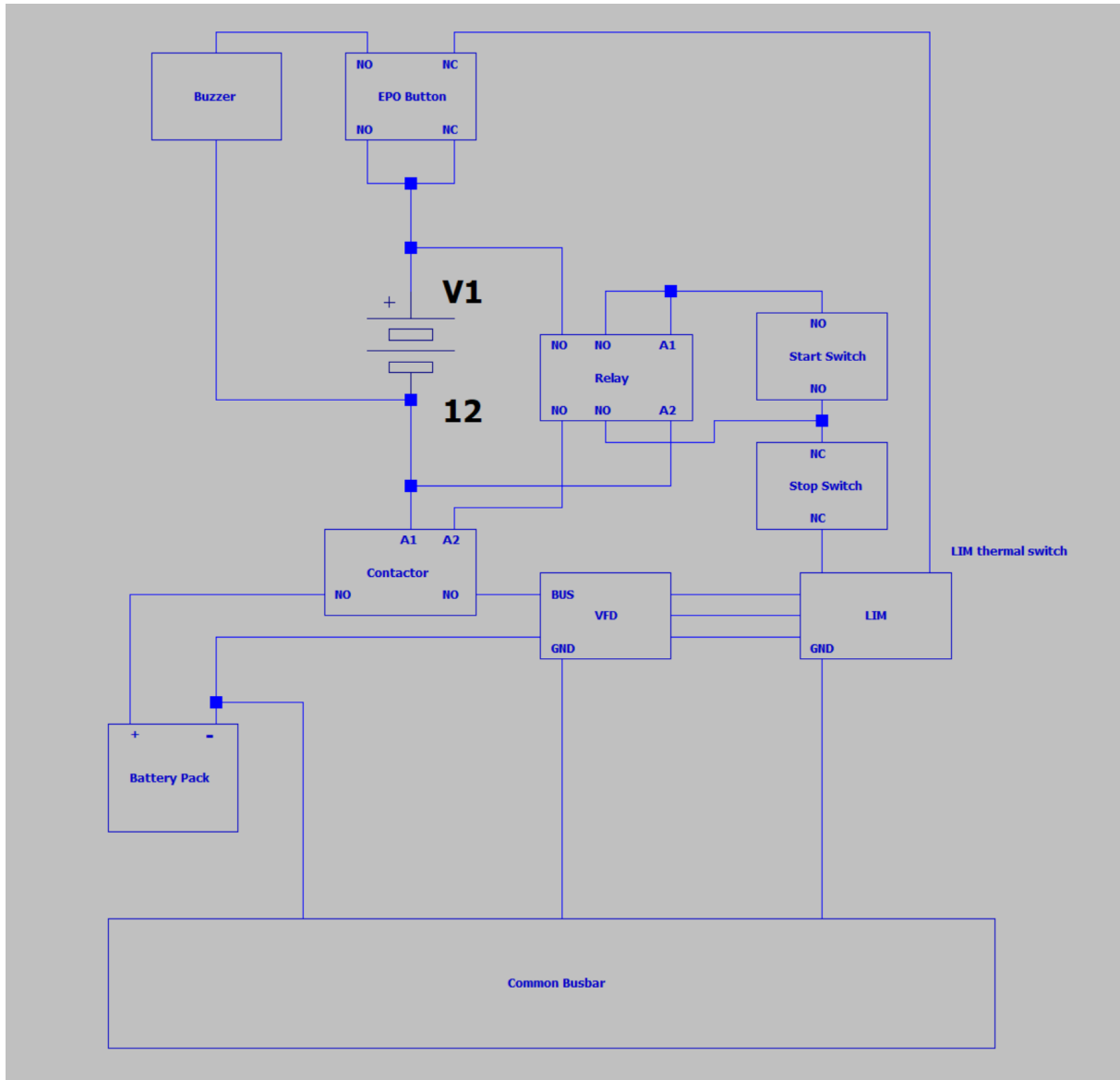


Figure 1: High Level Overview of Power Subsystem

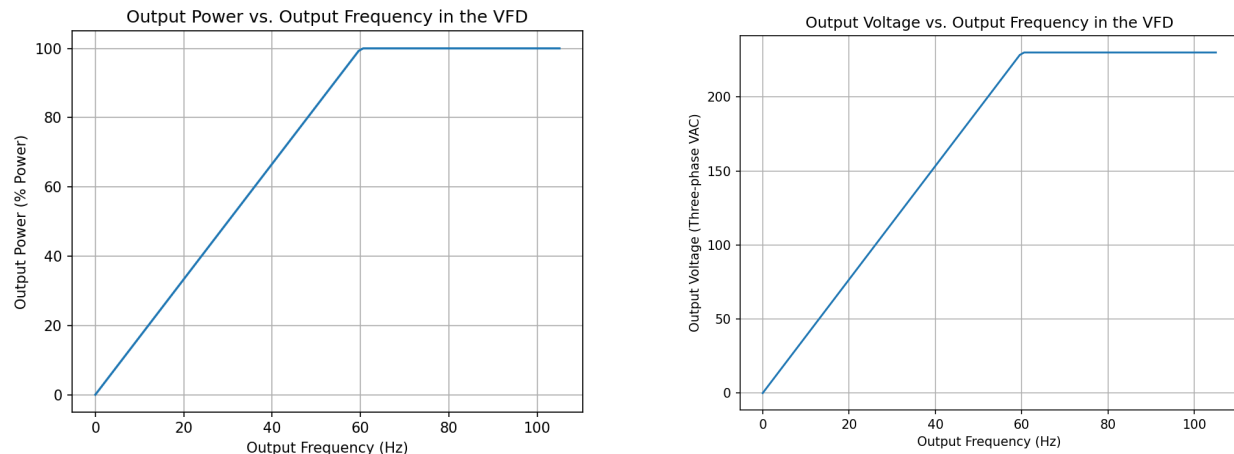


Figure 2: Power and Voltage vs Frequency for VFD

Table 1: Battery Cell Data

Battery	A123 LiFePO4 26650 Rechargeable Cell
Nominal Voltage	3.25V +/- 0.05V Nominal, 3.2V Average
Discharging current	Maximum Continuous Discharging: 50A, 20C rate Maximum Impulse Discharging (< 10 sec): 120A, 48.0C rate
Temperature Range	Charge and Discharge: -30°C to 55°C Storage: -40°C to 60°C
Dimensions(DxH)	26mm(1.0") x 65.15 mm(2.6")
Weight	2.9Oz (76 grams)

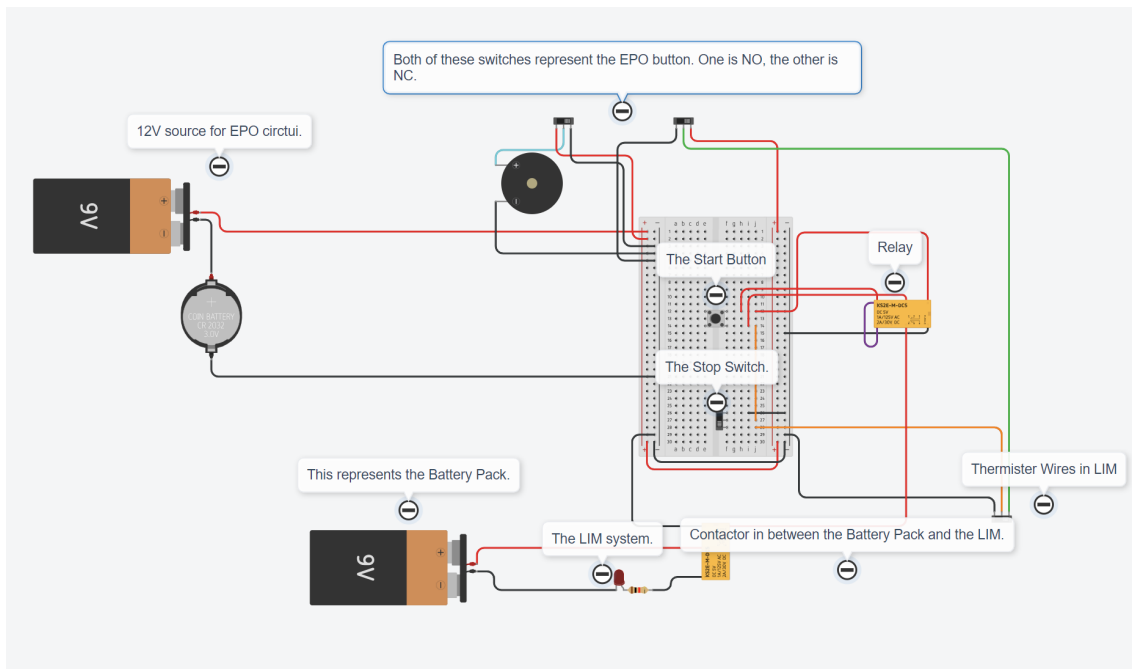


Figure 3: EPO Circuit Schematic

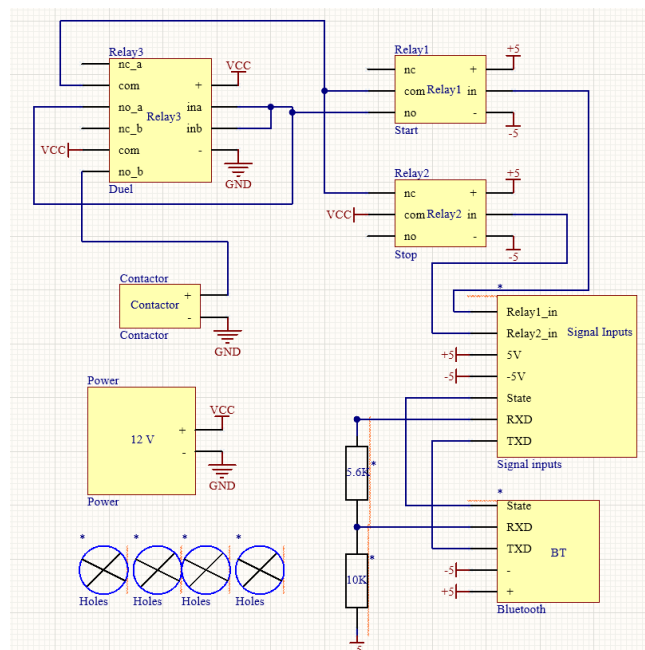


Figure 4: PCB Schematic

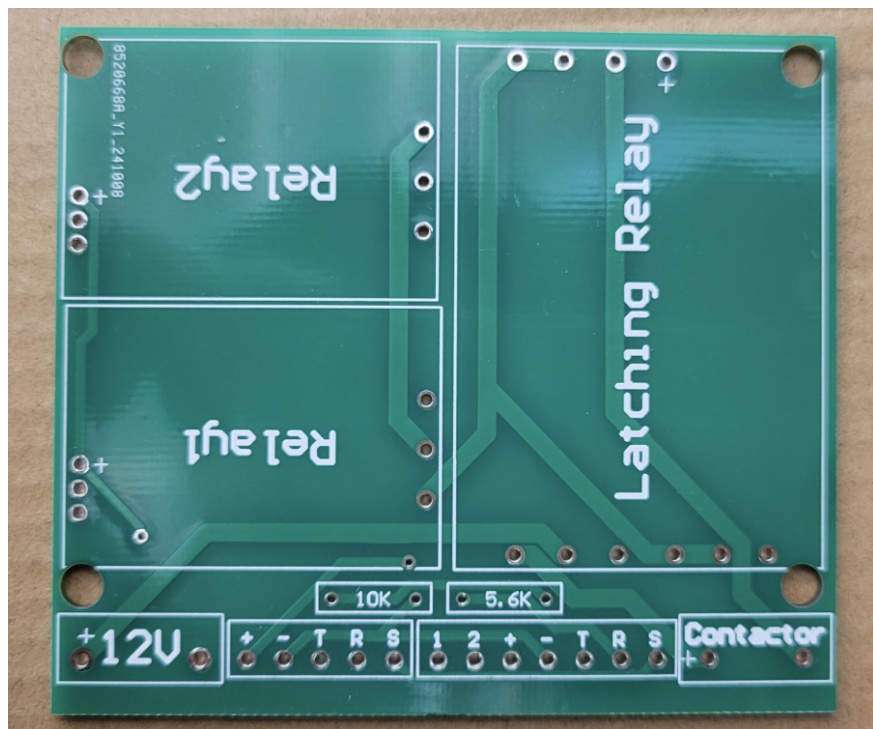


Figure 5: Image of Physical PCB Board

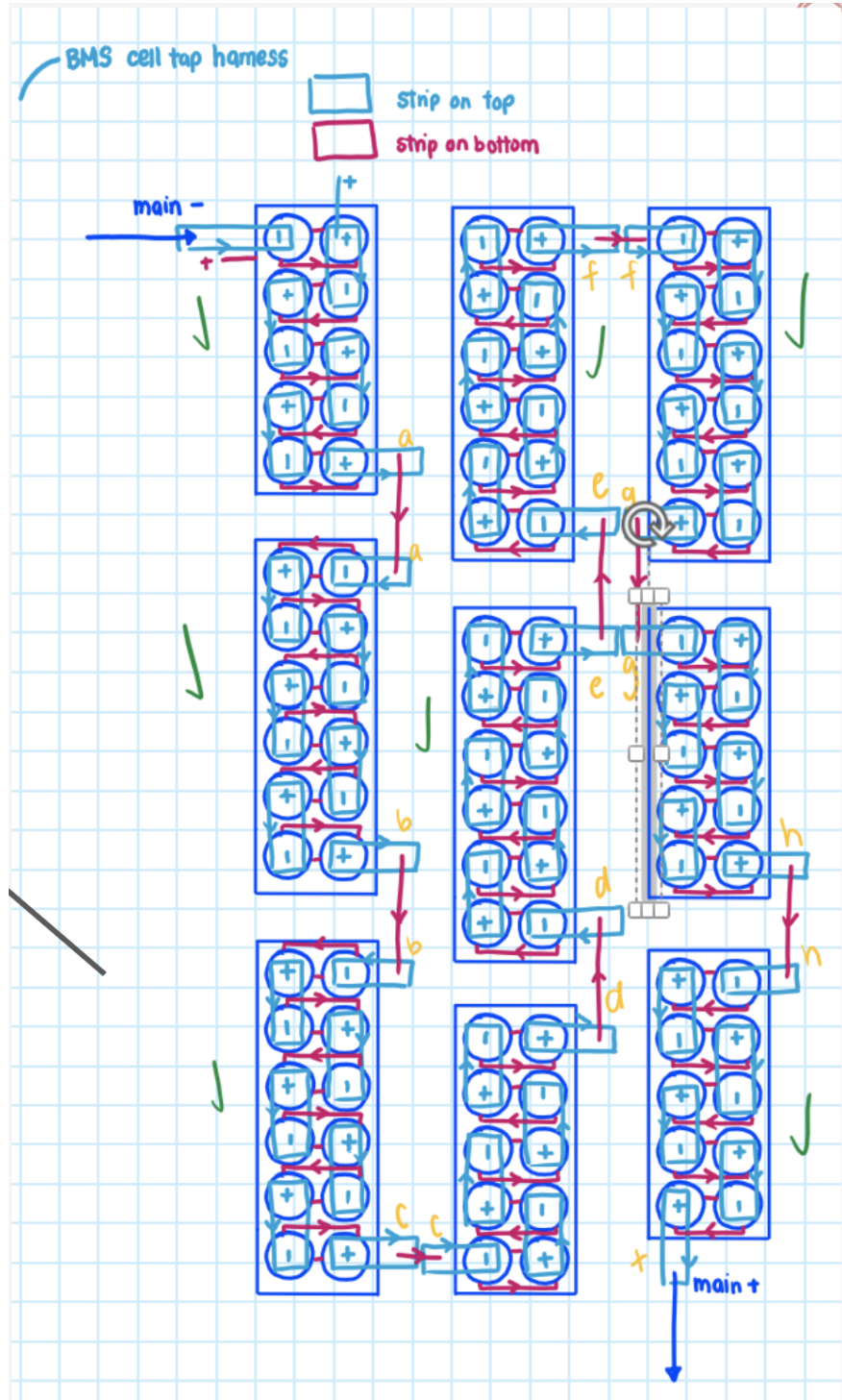


Figure 6: Layout of Battery Modules

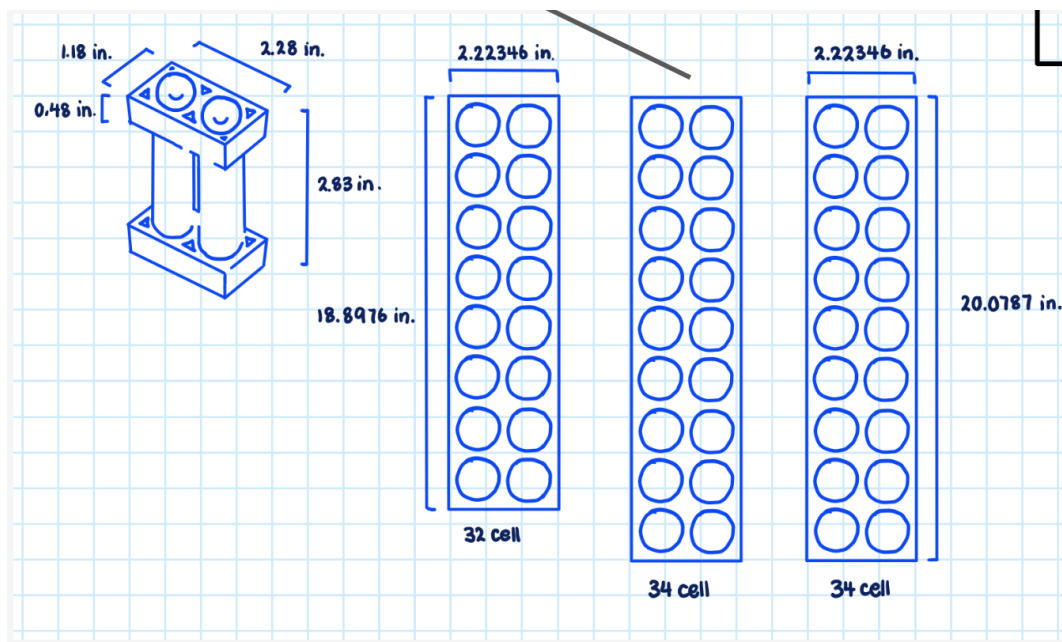


Figure 7: Battery Pack Specifications

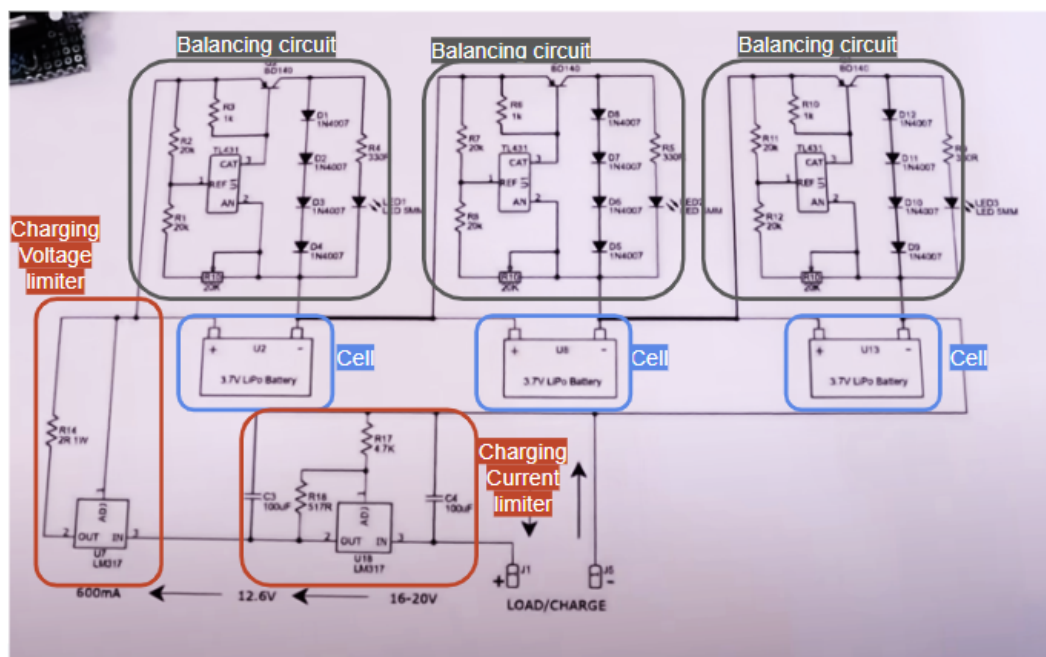


Figure 8: BMS Circuit Schematic